







Master of Science's thesis in Micro and Nanotechnologies for Integrated Systems (MNIS)

Academic year 2024/2025

Plasmonic Engineering of Superconducting Nanowire Single-Photon **Detectors**

Federica Marinelli

Student ID: 322876 Academic Supervisors:

Prof. Marco Colangelo – Northeastern University Prof. Fabrizio Giorgis – Politecnico di Torino

Acknowledgments

First and foremost, I would like to thank Prof. Marco Colangelo for welcoming me into his laboratory, for believing in me, and for teaching me how to carry out a project from start to finish. His trust has continually grown, making me more responsible and independent along the way. Working under his supervision has been one of the most formative experiences of my academic journey.

I would also like to thank Prof. Fabrizio Giorgis, my supervisor at Politecnico di Torino, for his constant availability and for being an inspiring mentor.

Thanks to my colleagues Kartikey Agarwal, Francesco Venza, and Rania Alshawabkeh for making the NSL lab such a stimulating environment. I am grateful for your collaboration, for all the insightful discussions on our projects, and for your help, especially during the experimental phase.

A special thank you to Lorenzo Barbati for being an exceptional colleague over these six months. Thank you for all your professional and personal support, this experience would not have been the same without you.

Thanks to all the undergraduates who were part of the lab during these months and contributed to its growth, in particular Faith Degawa, Liam Kelly, and Evan Clifford.

I also wish to thank all the members of the NanoSI Institute at Northeastern University for the fruitful discussions, and especially Aurelio Venditti for his help during the final measurement phase described in this thesis.

Many thanks to the technicians of the Kostas Nanofabrication Laboratory at Northeastern University and MIT.nano at MIT for their support in developing the cleanroom fabrication process described in this work.

An enormous thank you to my family, Marianna Milano, Paolo Marinelli, and Roberto Marinelli, for always being by my side throughout this journey, for believing in me even in the hardest moments, and for understanding my choices, even when they took me six time zones away. Thanks also to the rest of my big family for making every time I come home a truly special moment.

Thank you to all my friends. To the Nano20 group, friends I met along this long path through Italy, France, and Switzerland, thank you for sharing both the stress and the beers. A special thanks to Lorenzo Aime for being a constant presence and a great support, for the countless dinners together. To all the wonderful people I met in Turin, especially Francesca Brovia for being not only a fantastic flatmate but also a special friend in New York. Thanks to Federico Arnaudo, Alessandro Memmolo, and Cesare Piemontese for being amazing study partners and friends.

To my friends from home, thank you Claudia Lattarulo for being a constant presence all these years, since high school. Thank you for seeing me for who I am, for sharing experiences even from afar, and for our long talks, during which you always manage to say exactly the right thing to make me feel better. I feel truly lucky to have you. Thank you Umberto Angelillo, Michela Tria, Daniela Caputo, Maria Antonietta Montenegro, and Pompeo Lippolis for the joy we share every time we meet, even after months apart, with endless stories and affection. Thank you Nicola Ciliberti for always being there, for being a wonderful person and a steady support. You are someone I know I can call at any hour of the day or night, and I hope the same is true for me.

To the friends I met in Boston, who made me feel at home even on another continent. In particular, I would like to thank Ilaria Campestrini, Giacomo Gobbo, and Nicole Sasso for being an incredible support network and for all the adventures we shared. I love you all very much.

Finally, thank you Davide Mondin for holding my hand through every step of this journey, for exploring Boston with me, and for being my biggest supporter. Thank you for making this experience truly unforgettable.

Abstract

Superconducting Nanowire Single-Photon Detectors (SNSPDs) are the most prominent and versatile technology for single-photon counting at near-infrared (NIR) wavelengths. Through the introduction of specialized superconducting materials, SNSPDs have also been demonstrated at mid-infrared (MIR) wavelengths.

However, reaching the same performances at this range remains an elusive goal. For example, traditional methods for enhancing optical absorption, such as optical cavities, are practically not suitable at longer wavelengths due to the large thickness required.

This thesis proposes a novel detector architecture that combines the resonant plasmonic perfect absorber effect with a fractal metasurface to achieve high-efficiency, broadband, and polarization-insensitive single photon absorption and detection in the MIR. This is achieved by using a superconducting niobium nanowire as both the photon-detecting element and the active absorber component, taking advantage of its plasmonic properties. Furthermore, we use a space-filling Gosper curve to excite multiple plasmonic resonances at different wavelengths, thereby exploiting the multiple scales inherent in fractal geometry. The fractal absorber is integrated with a reflective backplane and a thin dielectric spacer, forming a compact cavity structure optimized for MIR operation.

The optical simulations of the designed structure show an average absorption of approximately 82% across the 3–7 μm range. The fabrication process of the proposed detector was carefully designed. The most challenging step, electron-beam lithography, was successfully executed and optimized, enabling device fabrication and the completion of preliminary optical and electrical tests that validate its performance.

The proposed design enables compact, scalable detectors with potential impact in thermal imaging, quantum sensing, and mid-infrared molecular spectroscopy.

Contents

1 Introduction		oduction				
	1.1	Background on Superconducting Nanowire Single-Photon Detectors (SNSPDs)				
	1.2	Research Gap: MIR Absorption Limitations				
	1.3	Thesis Objectives and Structure				
	1.4	The NSL group, the KNMRC at Northeastern University and MIT.nano				
2	The	Theoretical Framework, Design, and Simulation				
	2.1	Fundamentals of Plasmonics for Enhanced Optical Absorption				
	2.2	Design Strategy and Motivation				
		2.2.1 Perfect Absorber Concept				
		2.2.2 Fractal Geometries for Broadband MIR Absorption				
	2.3	Optical Simulation Methods				
	2.4	Material Evaluation: NbTiN vs Nb				
		2.4.1 Material Properties and Optical Characterization				
		2.4.2 Evaluation of Absorption Performance				
	2.5	Design and Layout Optimization of Fractal SNSPDs				
		2.5.1 Design and Pattern Optimization				
		2.5.2 Absorption Efficiency and Performance Metrics				
3	Ext	Experimental Fabrication and Characterization 2				
_	3.1	Nb Thin Film Deposition by Sputtering				
	3.2	Material Characterization				
	٥	3.2.1 Sheet Resistance Measurements				
		3.2.2 Critical Temperature Measurements				
		3.2.2.1 Cryogenic Setup				
		3.2.2.2 Results				
		3.2.3 Ellipsometry Measurements				
	3.3	Device Fabrication Process				
	3.4	Preliminary Device Performance Characterization				
	0.1	3.4.1 Cryogenic Setup				
		3.4.2 Electrical Characterization				
		3.4.3 Optical Characterization Using FTIR Spectroscopy				
4	Cor	aclusions and Outlook				
*	4.1	Summary of Main Results				
	$4.1 \\ 4.2$	v				
	4.2	Suggested Future Work				

List of Figures

1	Overview of the superconducting nanowire single-photon detector	(
2	Fractal nanowire width and step length	1.
3	Fractal and dielectric layer thicknesses	11
4	Fractal stages	12
5	Simulation setup overview.	13
6	Zoom on fractal nanowire and simulation grid	14
7	Comparison of optical properties	15
8	Absorption, reflection, and transmission spectra of fractal nanowire structures of	10
O	NbTiN and Nb	16
9	Electric-field intensity ($ E ^2$) distribution in the central cross-section of a nanowire	1(
9	made of NbTiN at different wavelengths	16
10	Electric-field intensity ($ E ^2$) distribution in the central cross-section of a nanowire	1(
10		1.5
11	made of Nb at different wavelengths	17
11	Absorption, reflection, and transmission spectra of Nb nanowire structures with a	10
4.0	thickness of 20 nm and linewidth of 40 nm.	18
12	Absorption dependence on the dielectric layer thickness	19
13	Effect of fractal structure thickness on absorption coefficient	20
14	Influence of the fractal step length on the absorption spectrum	21
15	Surface current density magnitude K and current streamlines for the two geometries	21
16	Impact of corner curvature on the absorption spectrum	22
17	Final optimized fractal design.	23
18	Absorption, reflection, and transmission spectra of the final optimized fractal design.	24
19	Comparison of absorption performance for TM and TE polarizations	24
20	Layout design of the fabricated fractal SNSPD	25
21	Schematic of the AJA magnetron sputtering chamber used for niobium thin-film	
	deposition.	26
22	3D Computer-Aided Design (CAD) of the cryostat for T_c measurements	28
23	Resistance vs. temperature curve for the Nb sample sputtered for 120 s	29
24	Resistance vs. temperature curve for the Nb sample sputtered for 240 s	29
25	Optical properties (refractive index and extinction coefficient) as functions of wave-	
	length extracted from ellipsometry measurements.	30
26	Ellipsometry-derived thickness vs. deposition time with linear fit, consistent with a	
	constant deposition rate	31
27	Preliminary simplified process for Nb patterning on SiO_2	32
28	Comparison of results obtained with negative resists	32
29	Example of high-quality HSQ fabrication	33
30	Comparison of HSQ exposure results	33
31	Complete fabrication process for the device	34
32	Schematic of the I–V measurement circuit	$\frac{3}{3}$
33	I–V characteristics of the 40 nm-wide nanowire device measured at 1.6 K	36
34	I-V characteristics of the 40 nm-wide nanowire device measured at 1.6 K	36
35	Comparison between simulated and experimental FTIR absorption spectra of the	30
39		25
	fabricated structures	37
T :1	of The late	
List	of Tables	
1	Comparison of absorption values in NbTiN vs. Nb	17
2	Comparison of current crowding metrics for sharp and rounded corners	22
3	Sheet resistance computed for different deposition durations	27
4	Thickness measured for different deposition durations	31
	±	

List of acronyms

Au Gold

CAD Computer-Aided Design

DC Direct CurrentDCR Dark-Count Rate

DUT Device Under Test

FDTD Finite-Difference Time-Domain

FTIR Fourier-Transform Infrared spectroscopy

 $I_{\rm c}$ Critical current

IDE Internal Detection EfficiencyLiDAR Light Detection and Ranging

LSPR Localized Surface Plasmon Resonance

MIR Mid-Infrared

Nb Niobium

NbN Niobium Nitride

NbTiN Niobium Titanium Nitride

NIR Near-Infrared

PEC Proximity Effect Correction

PECVD Plasma-Enhanced Chemical Vapor Deposition

PML Perfectly Matched LayerPSB Printed Sample Board

PVD Physical Vapor Deposition

QKD Quantum Key Distribution

RF Radio Frequency

RIE Reactive Ion Etching

 ${f RRR}$ Residual Resistivity Ratio

SDE System Detection Efficiency

SEM Scanning Electron Microscopy

Si Silicon

SiO₂ Silicon Dioxide

SNSPD Superconducting Nanowire Single-Photon Detector

 $T_{\rm c}$ Critical temperature

1 Introduction

1.1 Background on Superconducting Nanowire Single-Photon Detectors (SNSPDs)

Superconducting nanowire single-photon detectors (SNSPDs) have transformed photon counting in the optical and near-infrared (NIR) range by combining high detection efficiency, ultralow noise, and picosecond timing capabilities [1, 2]. They have applications in quantum information [3](long-distance QKD [4, 5], integrated photonics [6]), photonic computing [7], optical communications [8], LiDAR [9], spectroscopy [10], biomedical imaging [11], and astronomy [12]. Since their initial experimental demonstration in 2001 [13], showing that absorption of a single photon in a current-biased ultrathin niobium nitride (NbN) strip could generate a measurable voltage pulse via a transient resistive hotspot, SNSPDs have advanced from laboratory demonstrations to market-ready instruments combining near-unity efficiency with wafer-scale manufacturability[14].

Operating principles and detection physics

An SNSPD is typically a nanowire meander made of a superconducting material (5–10 nm thick and 50–150 nm wide) with a pixel area of about $10 \times 10 \ \mu m$ (Figure 1 [15]). It is cooled below its critical temperature T_C , which is the temperature threshold between the superconducting and normal states, and biased just below its critical current I_C , beyond which superconductivity is lost. Under these conditions, absorption of a single photon is sufficient to create nonequilibrium quasiparticles and phonons, which locally suppress superconductivity and form a resistive region called a hotspot. This resistive region expands due to different phenomena and diverts current to the readout circuit, producing a detectable voltage pulse. The hotspot then relaxes, and the device cools, resetting to the superconducting state.

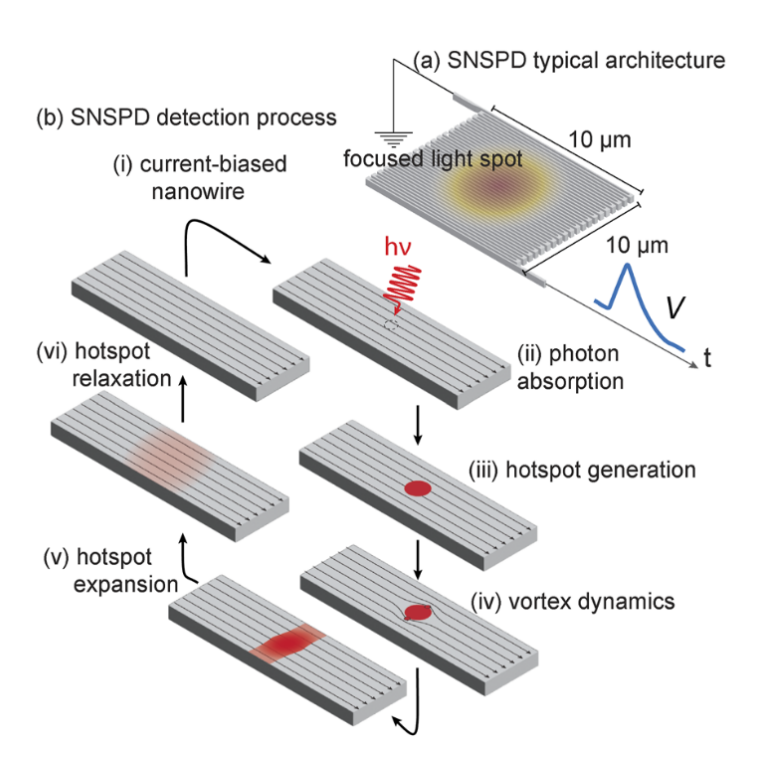


Figure 1: Overview of the superconducting nanowire single-photon detector. (a) Typical architecture of the SNSPD. This sketch omits elements of the optical cavity and electrical readout. A light spot is focused on a $10 \times 10 \ \mu m^2$ active area meander, leading to an output electrical pulse. (b) SNSPD detection process outlook. Reproduced with permission from [15]

Beyond the canonical hotspot picture, vortex-assisted mechanisms and coupled electro-thermal

dynamics refine the understanding of hotspot expansion, reset dynamics and the phenomenon of latching. When a photon is absorbed, it not only produces a localized cloud of quasiparticles but can also reduce the barrier that opposes vortex entry. This process lowers the energy cost for a vortex to form at the edge and cross the nanowire, creating a transient resistive path. The subsequent motion of vortices, together with the redistribution of the bias current around the perturbed area, governs the moment at which the device switches from the superconducting to the resistive state. At the same time, electro-thermal feedback, arising from the competition between Joule heating in the resistive region and heat transfer to the substrate, regulates the growth and relaxation of the normal domain [16].

A typical phenomenon that can occur is latching, namely the failure to reset when positive thermal feedback allows Joule heating in the normal region to exceed heat removal to the substrate during electrical recovery, leaving a persistent resistive segment. To avoid latching a better thermal coupling with the substrate or a slower electrical recovery, thanks to higher kinetic inductance or a series resistor, can be explored [17, 18].

Quantitative performance and fundamental trade-offs

Four metrics are usually defined to characterize system performance: system detection efficiency (SDE), dark-count rate (DCR), timing jitter, and reset (recovery) time. Their simultaneous optimization remains one of the central engineering challenges.

The SDE is the probability that the system detects an incident photon successfully. This parameter accounts for both the internal detection efficiency (IDE) and the optical losses arising from the non-unitary absorptance of the system. Optical cavities are often employed to increase the probability that a photon is absorbed by the detector, while the IDE represents the probability that an absorbed photon produces an electrical response. In the state of the art, this metric reaches up to 99.5% in the NIR with a niobium-titanium nitride (NbTiN) detector on a gold-mirror cavity [19].

The DCR is the number of registered detection events in the absence of illumination per unit time. This noise originates mainly from thermally activated vortex crossings and stray blackbody photons. State-of-the-art devices achieve DCR values as low as 10^{-7} cps for dark-matter applications [20].

The timing jitter measures the uncertainty in the recorded arrival time of a photon. It depends on both the detector and the readout circuitry and is a critical parameter for applications such as LiDAR. The current state-of-the-art record is 4.6 ps at 1550 nm wavelength, achieved by optimizing both a short nanowire and the experimental setup [21].

The reset time is the interval required for the detector to recover and become ready to register another photon. The maximum sustainable count rate is limited by recovery time $\tau_R \approx \frac{L_k}{R_L}$, where L_k is the kinetic inductance of the nanowire and R_L the load resistance of the circuit, as well as by the dynamics of the readout chain. These parameters must be carefully optimized, since reducing the reset time can increase the risk of latching. State-of-the-art implementations achieve count rates as high as 1.5 Gcps using an array of SNSPDs [2].

There are several trade-offs between these performance metrics. One important trade-off involves the active area of the detector. A larger area increases the SDE by enhancing optical absorption, but it also tends to degrade the timing jitter because the signal takes longer to propagate to the readout circuit. Conversely, a shorter nanowire can achieve very low jitter, but at the cost of a significantly reduced probability of photon absorption. Reducing the kinetic inductance by shortening the nanowire can also decrease the reset time and support higher count rates, but this often requires operating the device at a bias current closer to its critical value in order to maintain high detection efficiency. This operating point makes the nanowire more sensitive to dark count events. Future research will focus on optimizing the key trade-offs to realize a all-rounded detector technology [15].

1.2 Research Gap: MIR Absorption Limitations

Matching the NIR performance of SNSPDs at longer mid-infrared (MIR) wavelengths remains a central challenge. Many applications, such as spectroscopy [10] and astronomy [12], require MIR single-photon detection with high efficiency. Although unity IDE has been demonstrated deep into the MIR range (up to $\sim 10~\mu m$ [22], including large area meanders at 7.4 μm [23], and even 29 μm in WSi [24]) the field still lacks experimentally validated, high-absorptance optical stacks capable of translating this intrinsic sensitivity into high SDE across the 5–12 μm bands [25]. Most long-wavelength studies focus on IDE while deferring complete absorption/coupling engineering and full system-level SDE measurements [22, 23, 26]. In contrast, at short-MIR wavelengths ($\approx 2~\mu m$), dielectric-cavity designs combined with optimized fiber coupling have already yielded both high absorptance and high SDE, underscoring that at longer MIR wavelengths the dominant bottleneck is no longer intrinsic sensitivity, but rather optical absorption engineering [27–29]. Furthermore, without standardized long-MIR SDE metrology across well-defined passbands and numerical apertures, it remains difficult to compare absorber designs or to verify claimed system-level gains in this spectral region [30].

Beyond absorption, two additional factors limit MIR SNSPDs. First, the lower photon energies at long wavelengths push operation closer to the switching current threshold, increasing sensitivity to superconducting-film imperfections and bias-current instabilities [31, 32]. Second, higher black-body backgrounds in the MIR raise the system DCR and require advanced cryogenic filtering to maintain low-noise performance [33, 34].

Addressing these issues will require absorber architectures that are broadband, polarization-independent, and compatible with compact, scalable device integration to unlock the full system-level potential of MIR SNSPDs. This thesis targets precisely this challenge, exploring a novel design concept that merges broadband perfect absorption with subwavelength structural engineering to overcome the intrinsic limitations of traditional cavity-based approaches.

1.3 Thesis Objectives and Structure

The objective of this thesis is to design, model, and experimentally investigate a new architecture for SNSPDs capable of achieving broadband, polarization-insensitive, and high-efficiency operation in the MIR range. Building on the limitations identified in current absorption enhancement strategies, the proposed approach aims to integrate subwavelength and fractal-inspired structural engineering into a compact perfect absorber platform, optimized for the 3–7 μ m spectral band. This strategy directly addresses the current limitations of cavity-based absorbers at long wavelengths and targets the achievement of system-level performance metrics, particularly SDE, that match the best results in the NIR. By merging advanced optical absorption engineering with the intrinsic sensitivity of superconducting nanowires, this thesis seeks to enable MIR detectors suitable for demanding applications such as thermal imaging, quantum sensing, and molecular spectroscopy.

The rest of this thesis is organized as follows:

- Chapter 2 presents the theoretical framework, including plasmonic principles for enhanced absorption, simulation methodologies, and the rationale behind the proposed perfect absorber and fractal geometry approach. Material selection and design optimization strategies are also discussed.
- Chapter 3 describes the experimental implementation, from niobium thin-film deposition and material characterization to device fabrication. Preliminary performance characterizations are reported, including optical measurements via FTIR spectroscopy and critical current evaluation.
- Chapter 4 summarizes the main results, discusses the implications for MIR SNSPD technology, and outlines future research directions.

1.4 The NSL group, the KNMRC at Northeastern University and MIT.nano

This thesis was conducted within the Nano Structures Laboratory (NSL) at Northeastern University, led by Prof. Marco Colangelo. NSL's research culture, centered on superconducting thin films, nanofabrication, and quantum device concepts, provided the intellectual setting and day-to-day feedback that shaped the project's goals and methodology.

Micro and nanofabrication activities took place at Northeastern University and at MIT. On the Northeastern side, work was carried out in the Kostas Nanofabrication Laboratory, which supported the deposition and etching processes. Complementary process steps and high-resolution characterization were performed at MIT.nano, whose cleanroom and microscopy resources enabled rapid verification of process outcomes and design choices.

NSL's research environment guided the device concepts and the measurement strategy, while the combined toolsets at Northeastern and MIT enabled reliable fabrication and rapid feedback between design, process optimization, and characterization.

2 Theoretical Framework, Design, and Simulation

2.1 Fundamentals of Plasmonics for Enhanced Optical Absorption

Plasmonic phenomena, arising from the collective oscillation of free electrons in metallic nanostructures, provide a powerful method to enhance optical absorption beyond the limits of conventional materials. This effect becomes possible because, in metals, the real part of the dielectric permittivity is negative at optical and infrared frequencies [35]. In this regime, light cannot propagate freely inside the metal, but instead couples to the oscillation of surface charges at the interface between the metal and a dielectric, forming what is known as a surface plasmon [36].

When the metallic structure has dimensions comparable to or smaller than the wavelength of light, these oscillations become localized, creating strong resonances called localized surface plasmon resonances (LSPRs). Around these resonant regions, the electromagnetic field can be concentrated into very small volumes, forming so-called "hotspots" where the field intensity is orders of magnitude higher than that of the incident wave. This extreme field localization significantly enhances the light–matter interaction, making plasmonic structures very effective in increasing absorption even in thin metallic layers where it would normally be weak [37].

By carefully designing the geometry of a nanostructure it is possible to tune the plasmonic resonance over a wide spectral range and control how the energy is distributed on the surface. In the architecture proposed in this thesis, the idea is to apply plasmonic engineering to achieve strong absorption over a broad wavelength range by exploiting two key concepts: the perfect absorber and the use of fractal geometries, which enable the excitation of multiscale plasmonic modes.

2.2 Design Strategy and Motivation

2.2.1 Perfect Absorber Concept

A perfect absorber is a structure designed to capture nearly all incident electromagnetic radiation by minimizing both reflection and transmission [38]. In general, the absorption A can be expressed as:

$$A(\lambda) = 1 - R(\lambda) - T(\lambda),\tag{1}$$

where $R(\lambda)$ and $T(\lambda)$ are the wavelength-dependent reflection and transmission, respectively. In a perfect absorber, the idea is to suppress reflection and transmission to achieve near-unit absorption.

From an electromagnetic perspective, perfect absorption occurs when the input impedance of the nanostructure matches the impedance of free space.

$$Z_{\rm in} = Z_0 \quad \Rightarrow \quad R = \left| \frac{Z_{\rm in} - Z_0}{Z_{\rm in} + Z_0} \right|^2 \approx 0.$$
 (2)

In literature it has been demonstrated that thin superconducting nanowires combined with a dielectric spacer and a metallic backreflector could be used as a perfect absorber [39]. The nanowire supports localized plasmonic modes that concentrate the electric field in the absorbing material, while the backreflector suppresses transmission. The dielectric layer can be tuned to adjust the phase of reflected waves, effectively controlling Z_{in} to achieve impedance matching over the desired spectral range.

The principles demonstrated in these nanowire absorbers inspire the design strategy explored in this thesis. Specifically, the concept of a perfect absorber is extended to multi-scale, space-filling structures to achieve broadband absorption in the mid-infrared while maintaining a compact footprint suitable for practical device integration.

2.2.2 Fractal Geometries for Broadband MIR Absorption

Following this design strategy, fractal geometries are employed to realize broadband absorption. Their self-similar structure supports resonances at multiple length scales, enabling interaction with a wide range of wavelengths. Among the various fractal designs, the Gosper curve has proven especially effective for MIR applications, as demonstrated in the work by *Broadband mid-infrared perfect absorber using fractal Gosper curve* [40]. This study served as a primary inspiration for the design of the nanowire structures in this work.

The fractal parameters were initially taken from the literature and then optimized for the specific structures considered here, as will be discussed in detail in the design section 2.5. Figures 2 and 3 illustrate the key geometrical parameters of the fractal: the width and step length of the nanowire, and the thicknesses of the fractal and the dielectric layer, respectively.

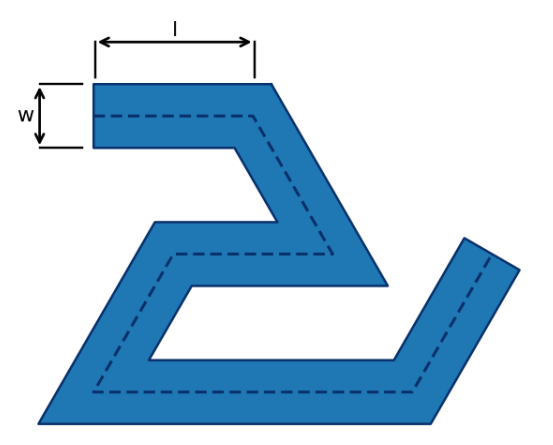


Figure 2: Schematic illustration of the fractal nanowire showing the key geometrical parameters: the nanowire width (w) and the step length of the fractal (l).

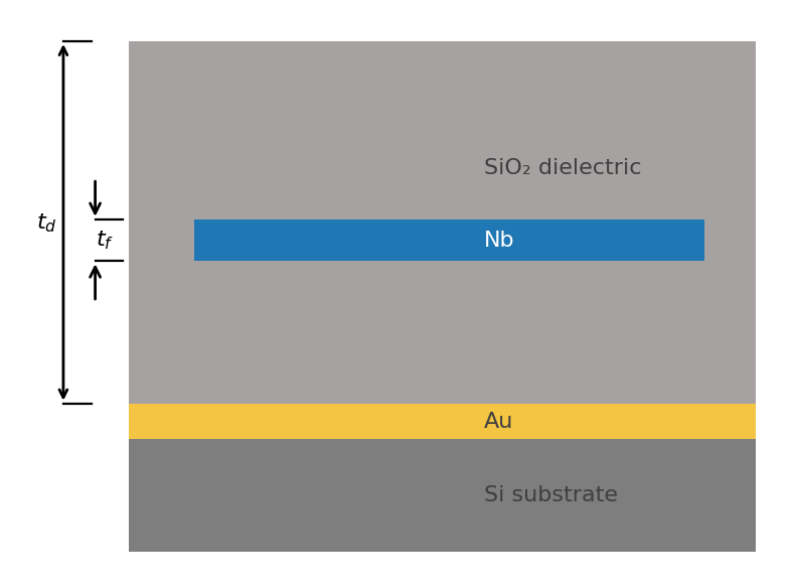


Figure 3: Cross-sectional view of the fractal nanowire structure, illustrating the thickness of the nanowire (t_f) and the dielectric layer (t_d) .

Several fractal stages were considered, each increasing the overall size of the structure, as

illustrated in Figure 4. To achieve plasmonic excitation, a collective effect over the structure is required, as noted in the literature where periodic boundary conditions were used to mimic an infinite array. In this work, a sufficiently large fractal, corresponding to stage 5, was selected so that the Gaussian source would effectively perceive it as an "infinite" structure, ensuring that plasmonic modes could be excited across the entire fractal.

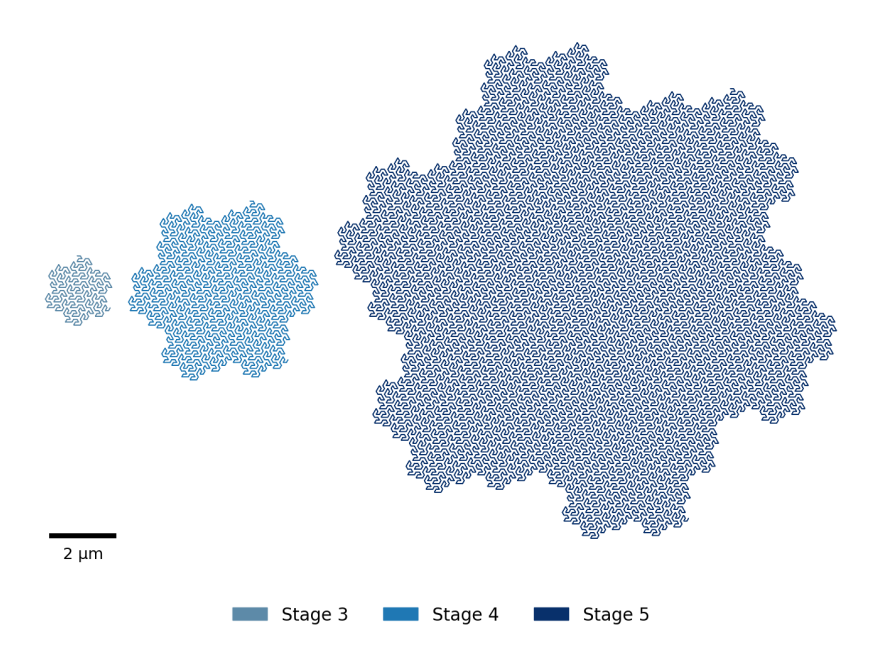


Figure 4: Illustration of several fractal stages considered in this work. Each stage increases the overall size of the structure. Stage 5 was selected for the simulations in this work.

2.3 Optical Simulation Methods

Optical simulations in this work were performed using Tidy3D, a finite-difference time-domain (FDTD) solver. FDTD is a numerical method that discretizes Maxwell's equations in both space and time, allowing for the direct calculation of electromagnetic field propagation through complex geometries. The FDTD approach is particularly suited for studying nanostructures, as it can capture resonant effects, plasmonic behavior, and near-field distributions with high accuracy.

The simulation setup remained essentially unchanged throughout all the optical simulations presented in this thesis. Figure 5 shows a vertical cross-section of the simulation domain, highlighting the main components: a gold backreflector at the bottom, a SiO_2 layer above, and the fractal nanowire structure positioned at the center. For gold [41] and SiO_2 [42], optical constants from the literature were used.

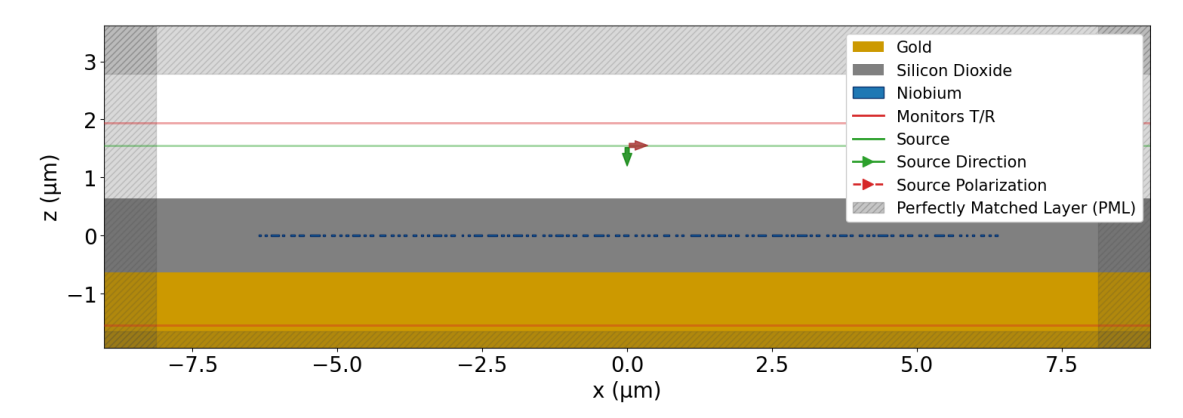


Figure 5: Vertical cross-section of the FDTD simulation setup. The gold backreflector is shown at the bottom, a SiO₂ above, and the fractal nanowire positioned at the center. A Gaussian source with a 5 μ m spot is centered on the nanowire, with propagation direction and polarization indicated. Two field monitors are placed above and below the structure to measure reflection, transmission, and absorption.

A Gaussian source with a spot size of 5 μ m was chosen to mimic the excitation from an optical fiber. In the figure, the source is clearly centered on the nanowire, with the propagation direction and polarization indicated. Two field monitors were placed in the simulation: one above the structure and one below, enabling the calculation of reflection, transmission, and, consequently, absorption.

Perfectly matched layer (PML) boundary conditions were applied on all boundaries to simulate an open system and prevent unphysical reflections. PMLs act as artificial absorbing layers that allow outgoing waves to exit the simulation domain without reflection, effectively mimicking an infinite space.

Figure 6 shows a zoomed-in view near the fractal nanowire. The discretization grid is clearly visible and sufficiently fine to accurately resolve the features of the fractal geometry, ensuring reliable calculation of field distributions and absorption.

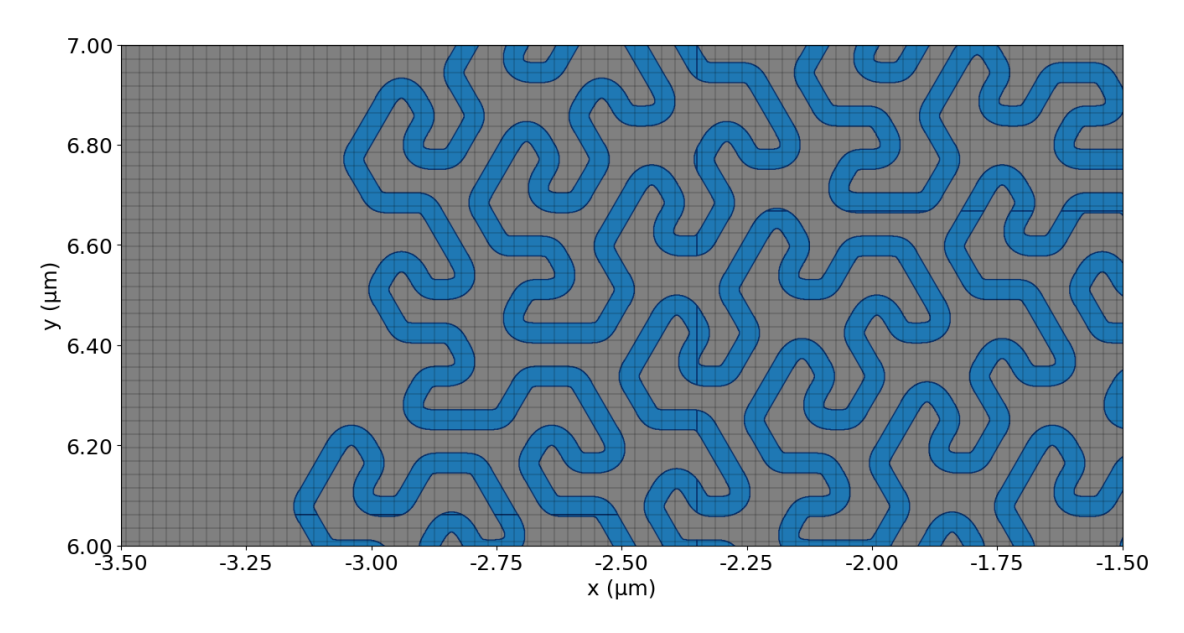


Figure 6: Zoomed view of the fractal nanowire region, showing the discretization grid used in the FDTD simulation.

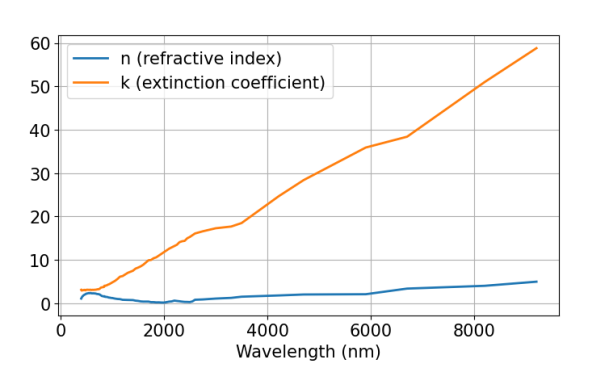
2.4 Material Evaluation: NbTiN vs Nb

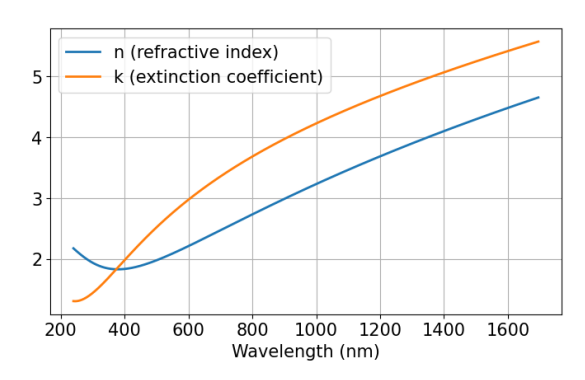
2.4.1 Material Properties and Optical Characterization

The choice of materials, as the first step in designing the fractal nanowire structure, focused on two candidates, NbTiN and Nb, selected for their relevance in SNSPDs and potential plasmonic behavior in the MIR.

NbTiN is the most widely used material for SNSPDs thanks to its high critical temperature and robustness, and its partially plasmonic character motivated its inclusion in this study. Nb, although less common for SNSPD fabrication, is a pure metal with strong plasmonic properties, making it an interesting candidate for broadband absorption when combined with complex geometries.

The optical constants of the two materials are shown in Figure 7.





- (a) Nb optical constants from literature at 4.2 K
- (b) NbTiN optical constants measured via spectroscopic ellipsometry

Figure 7: Optical properties of the materials considered in this study: (a) Nb refractive index n and extinction coefficient k from literature at 4.2 K [43], (b) NbTiN n and k measured experimentally via ellipsometry.

For NbTiN, reliable data are scarce in the literature, as its dielectric function is strongly dependent on stoichiometry and deposition conditions. Therefore, NbTiN films were fabricated by Lorenzo Barbati (NSL group) and their optical response measured experimentally via spectroscopic ellipsometry; however, the detailed characterization procedure is discussed in the section 3.2.3 for Nb, not NbTiN. The method applied to Nb is the same as for NbTiN, but here it is presented separately because the measurements were performed on Nb films deposited by the author. For preliminary studies, Nb optical data were first taken from established literature at 4.2 K to provide an initial estimate of the dielectric function [43]. This careful assessment of material properties provided the foundation for the subsequent analysis of absorption in fractal and meander nanowire geometries.

2.4.2 Evaluation of Absorption Performance

Based on the preliminary assessment of the optical properties of NbTiN and Nb, optical simulations of nanowire structures with fractal geometries were performed using Tidy3D. The goal was to investigate how the combination of material plasmonic behavior and complex geometry affects broadband absorption in the MIR.

Figure 8 summarizes the simulated absorption, reflection, and transmission spectra of the fractal nanowire structures made of NbTiN and Nb. The Nb sample exhibits overall higher absorption, with an average value of about 85% between 3-7 μ m, compared to approximately 68% for the NbTiN structure. Despite the partial plasmonic character of NbTiN, its lower absorption suggests that the apparent broadband response mainly originates from cavity effects rather than genuine plasmonic enhancement.

This interpretation is confirmed by the electric-field distributions shown in Figures 9 and 10. In the NbTiN case, the field is weakly confined within the nanowire and largely distributed in the surrounding cavities, consistent with a cavity-driven absorption mechanism. In contrast, the Nb structure shows stronger field localization and well-defined hotspots in the MIR range, particularly around 5.5 μ m and 6 μ m, indicating a true plasmonic contribution to enhanced absorption.

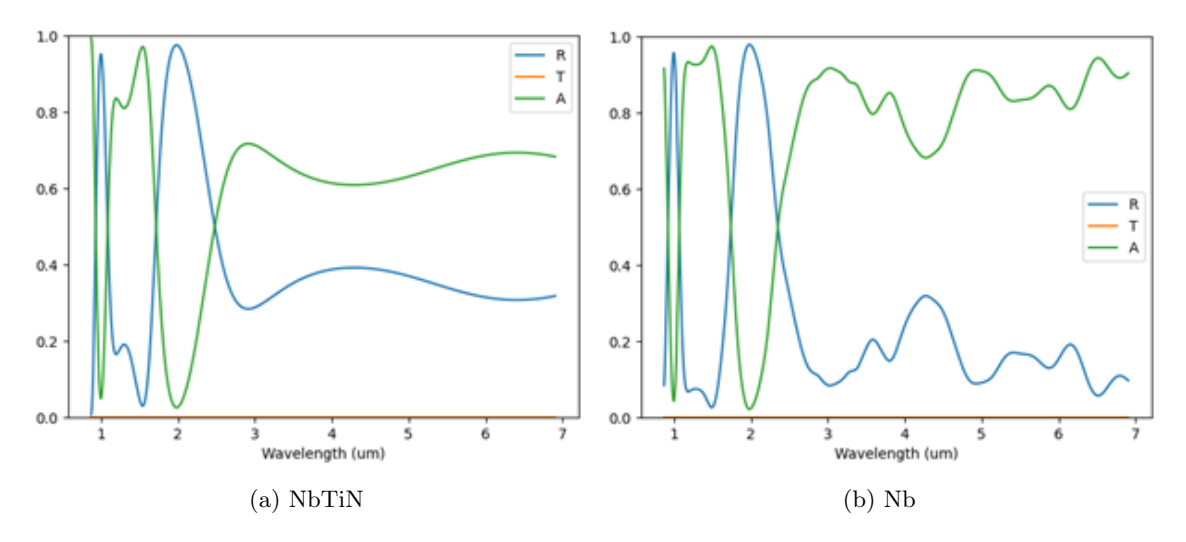


Figure 8: Absorption, reflection, and transmission spectra of fractal nanowire structures with a thickness of 20 nm and linewidth of 40 nm. (a) NbTiN. (b) Nb.

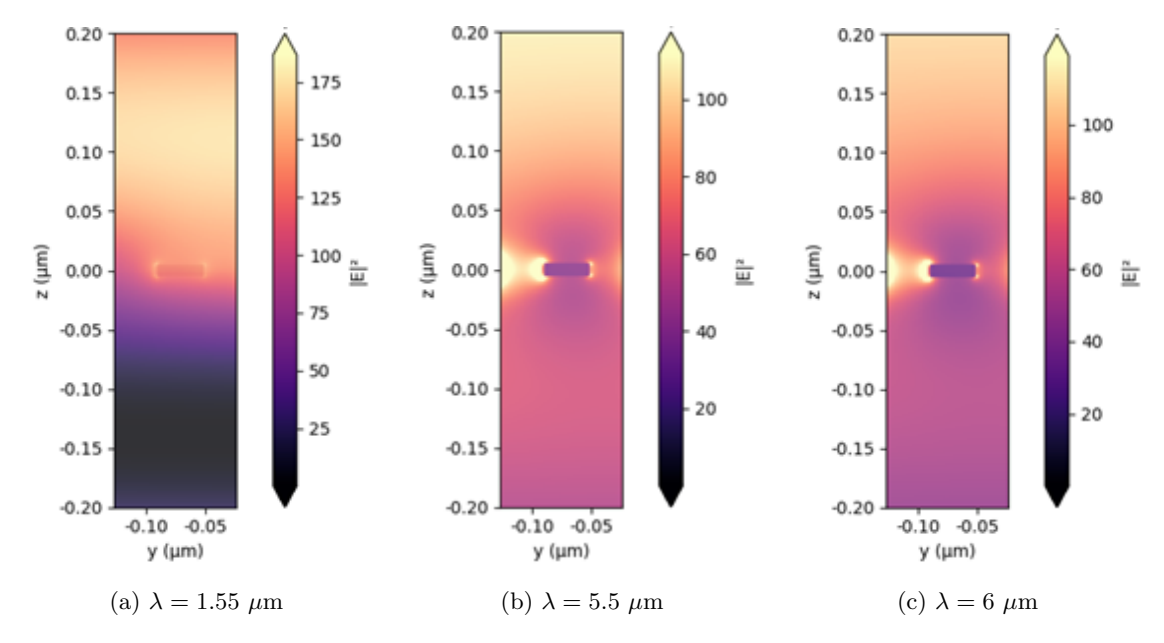


Figure 9: Electric-field intensity ($|E|^2$) distribution in the central cross-section of a nanowire made of NbTiN at different wavelengths: (a) 1.55 μ m, (b) 5.5 μ m, and (c) 6 μ m.

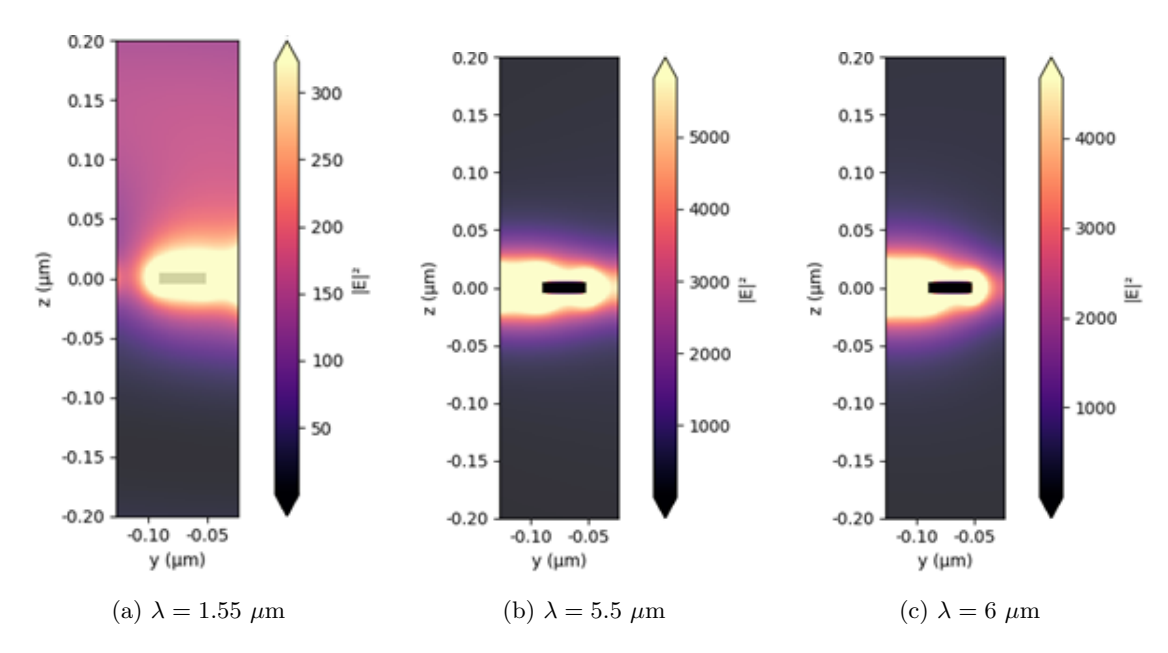


Figure 10: Electric-field intensity ($|E|^2$) distribution in the central cross-section of a nanowire made of Nb at different wavelengths: (a) 1.55 μ m, (b) 5.5 μ m, and (c) 6 μ m.

The absorption was quantified by integrating the field over a cross-section of the nanowire using the equation:

$$P_{\text{abs}} = \frac{1}{L} \int_{S} \frac{1}{2} \,\omega \,\varepsilon_0 \,\text{Im}[\varepsilon_{\text{mat}}] \,|\mathbf{E}|^2 \,dS \quad [W/\mu\text{m}],\tag{3}$$

where S denotes the cross-sectional area of the nanowire, $|\mathbf{E}|^2 = |E_x|^2 + |E_y|^2 + |E_z|^2$ is the local electric-field intensity, ε_0 is the vacuum permittivity, $\mathrm{Im}[\varepsilon_{\mathrm{mat}}]$ is the imaginary part of the material permittivity at the given frequency, ω is the angular frequency, and L is the length of the nanowire along the propagation direction. This expression represents the average power absorbed per unit length in the nanowire, and the results are summarized in Table 1. Nb achieves consistently higher absorption values than NbTiN, confirming that the combination of Nb's plasmonic properties with the fractal layout is responsible for the enhanced broadband performance. Although Nb is less commonly used in SNSPDs due to generally lower device performance compared to nitrides, its strong plasmonic behavior makes it a suitable choice for the objectives of this study.

Wavelength (μm)	Power absorbed in NbTiN (W/ μ m)	Power absorbed in Nb (W/ μ m)
1.55	0.0120	0.0152
5.5	0.0043	0.0409
6	0.0037	0.0349

Table 1: Average power absorbed per unit length in NbTiN and Nb nanowire structures at selected wavelengths in the MIR, expressed in W/ μ m. Nb shows significantly higher absorption, particularly at longer wavelengths, highlighting the effect of plasmonic enhancement in the fractal geometry.

Once Nb was selected as the material, an additional optical simulation was performed to compare the fractal geometry with the conventional meander design, keeping the nanowire width fixed at 40 nm and the pitch at 200 nm. As shown in Figure 11, the two geometries exhibit markedly different optical responses. The meander structure presents three absorption peaks in the NIR region, associated with resonant modes. In contrast, the fractal geometry displays a broadband absorption spectrum that extends well into the MIR, with overall higher absorption values across the entire range. This behavior confirms the ability of the fractal design to efficiently excite multiple resonances at different wavelengths, leading to a greater level of absorption in comparison to the conventional meander layout.

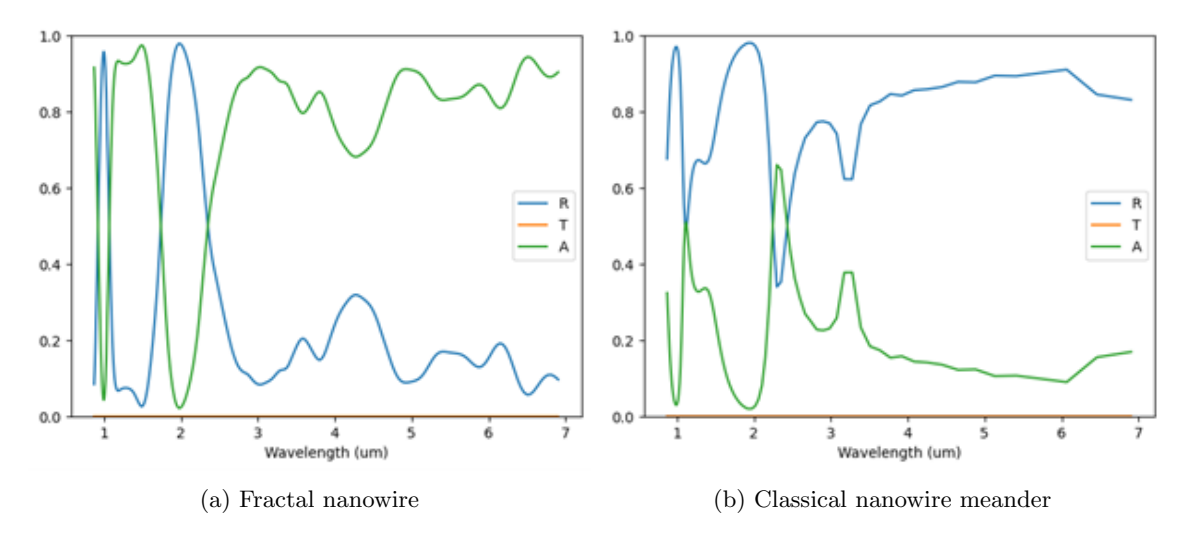


Figure 11: Absorption, reflection, and transmission spectra of Nb nanowire structures with a thickness of 20 nm and linewidth of 40 nm. (a) Fractal geometry. (b) Classical nanowire meander.

2.5 Design and Layout Optimization of Fractal SNSPDs

2.5.1 Design and Pattern Optimization

Once the material to be used was selected and an enhancement in absorption within the MIR range was demonstrated, the subsequent step involved the optimization of the various geometrical parameters in order to achieve the best possible performance in the MIR. This optimization process was carried out while taking into account both the fabrication constraints and the operational requirements necessary for the proper functioning of the nanowire as an SNSPD. The simulations were performed with Tidy3D, using as optical properties for Nb the ones experimentally extracted by ellipsometer measurements shown in the section 3.2.3.

Dielectric thickness

The first parameter investigated to optimize the absorption spectrum in the MIR range was the thickness of the dielectric layer. This parameter plays a crucial role in determining the wavelengths at which the structure exhibits the perfect absorber condition. Specifically, the layer between Au and Nb acts as a resonant electromagnetic cavity, supporting multiple overlapping resonances within the MIR range, while the upper layer serves to match the impedance between the Gosper resonator and free space.

In the simulations, all other geometrical parameters were kept constant in order to isolate the effect of the varying parameter. Specifically, the fractal thickness was fixed at 20 nm, the step length at 100 nm, and the nanowire width at 40 nm.

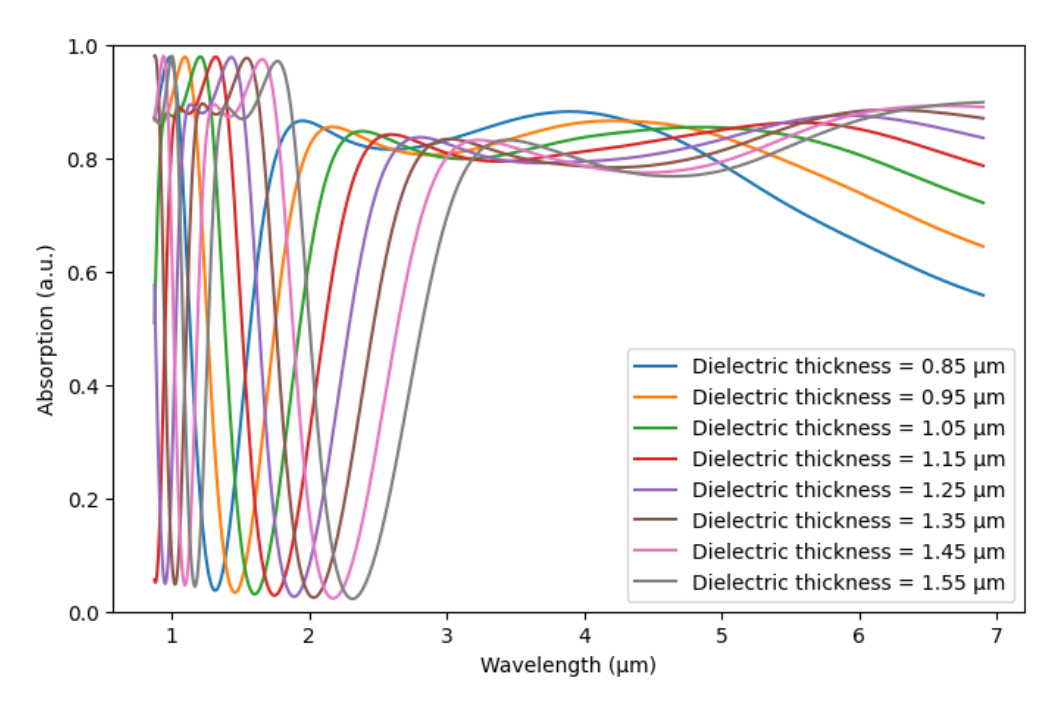


Figure 12: Absorption dependence on the dielectric layer thickness, with a fractal structure thickness of 20 nm, a step length of 100 nm, and a nanowire width of 40 nm.

A design choice made in this work, consistent with approaches reported in the literature [40], was to adopt a symmetric configuration, placing the fractal structure at the center of the dielectric layer. The total SiO₂ thickness was varied from 0.85 μ m to 1.55 μ m, a range over which a clear enhancement of absorption can be observed within the 3–7 μ m spectral window. As shown in Figure 12, it is interesting to note that, as expected, increasing the dielectric thickness results in a redshift of the absorption peaks and a gradual broadening of the bandwidth. This behavior arises from the change in the wavelengths at which multiple plasmonic modes occur within the structure.

Moreover, varying the dielectric thickness modifies the overall impedance of the structure, leading to a match of impedance with the free space at a different frequency [44].

By averaging the absorption over the 3–7 μm range, it was observed that the absorption remained nearly constant between 1.05 μm and 1.35 μm . Therefore, a dielectric thickness of 1.35 μm was selected, as it also exhibits a distinct absorption peak around 1.55 μm , a key wavelength for SNSPD operation. Consequently, this choice provides an advantage for future experimental tests performed using lasers operating at this wavelength.

Fractal thickness

The second parameter analyzed was the thickness of the fractal structure. The thickness was varied from 5 nm to 40 nm to study its influence on the absorption behavior. Increasing the Nb thickness leads to an enhancement of the peak intensity, which is consistent with the fact that this material accounts for most of the absorption. A thicker Nb layer increases the effective volume of the absorbing medium, resulting in a stronger and slightly broader absorption response.

However, this parameter must be optimized by considering the operational requirements of an SNSPD. In such detectors, very thin superconducting films are typically preferred to ensure efficient hotspot formation as well as thermal feedback and fast recovery times. As shown in Figure 13, while increasing the Nb thickness improves the overall absorption and produces a flatter spectral response, excessively thick layers could compromise proper detector performance. For this reason, a thickness of 20 nm was selected as the optimal trade-off. This value provides a high absorption level, only slightly lower than that achieved with thicker films, while remaining compatible with the reduced nanowire width used in this design and ensuring reliable SNSPD operation.

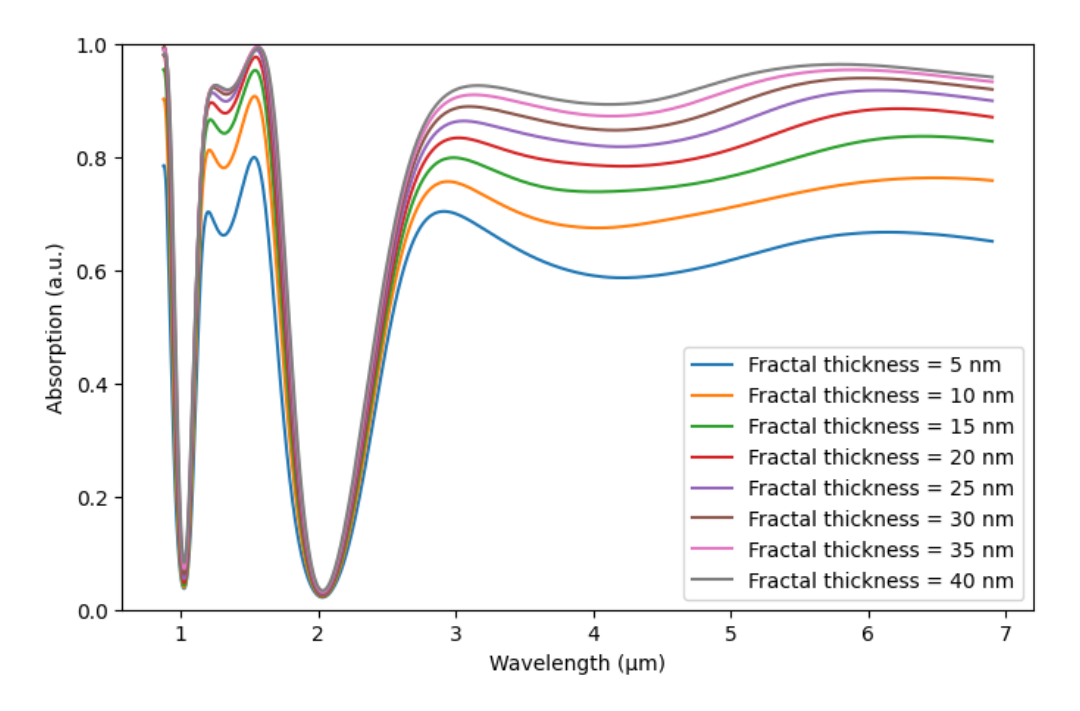


Figure 13: Effect of the fractal structure thickness on absorption coefficient, with a fixed dielectric layer thickness of 1.35 μ m, a step length of 100 nm, and a nanowire width of 40 nm.

Fractal step length

Another parameter considered is the fractal step length, which was varied from 80 nm to 200 nm. It should be noted that the lower limit is constrained by the resolution capabilities of electron-beam lithography (EBL). As shown in Figure 14, for larger step lengths, the fill factor of the fractal decreases and there is more spacing between different fractal segments. This results in a weaker resonance and, consequently, reduced absorption. The optimal value was initially 80 nm, which

was the target for the device. However, multiple EBL tests revealed that this resolution could not be reliably achieved, and therefore the final device was fabricated with a step length of 100 nm.

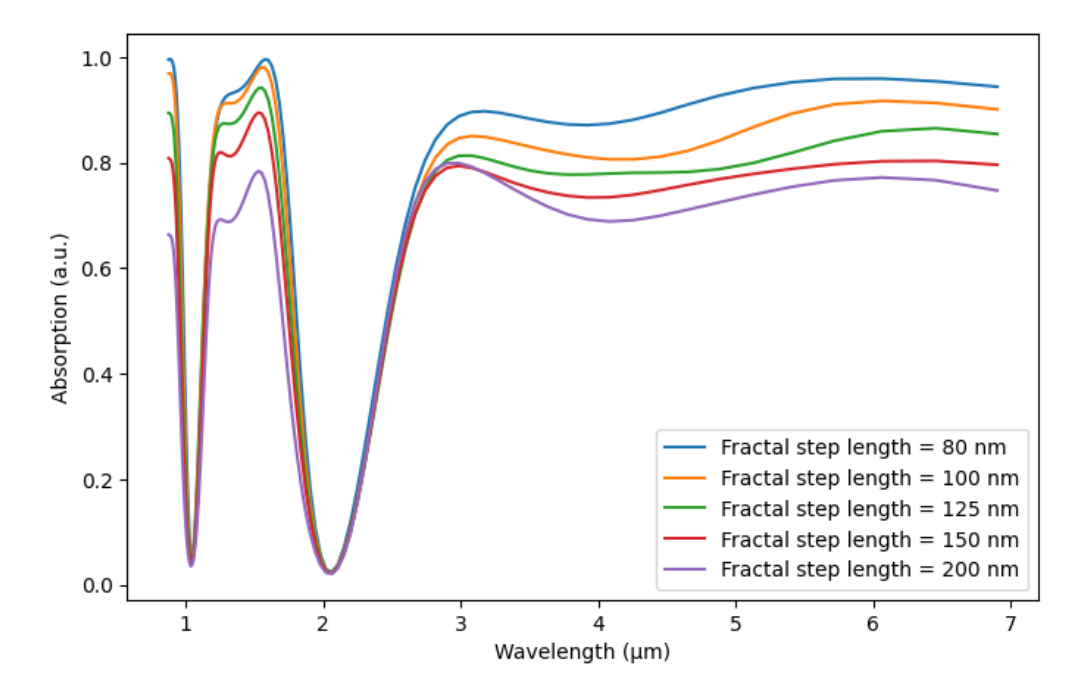


Figure 14: Influence of the fractal step length on the absorption spectrum, with a fixed dielectric layer thickness of 1.35 μ m, a fractal thickness of 20 nm, and a nanowire width of 40 nm.

Corners

Another parameter examined in detail is the roundness of the structure's corners. First, the limitations imposed by conventional EBL were considered, as perfectly sharp vertices are rarely achievable. At the tens-of-nanometer scale, e-beam proximity effects due to forward and backscattering inevitably broaden features, and subsequent pattern-transfer steps introduce additional corner rounding.

Since the resonant structure also serves as the active detector nanowire, PyTDGL was employed to evaluate how geometry influences the superconducting behavior. PyTDGL is a Python package that solves the time-dependent Ginzburg–Landau equations for thin superconducting films studing the superconductive properties.

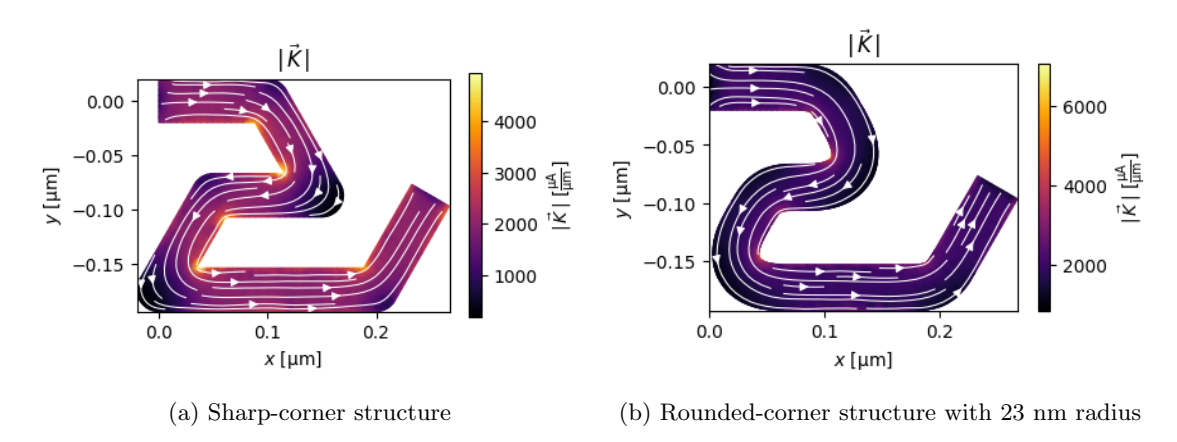


Figure 15: Surface current density magnitude K and current streamlines for the two geometries: (a) sharp-corner structure and (b) rounded-corner structure with 23 nm radius.

A representative section of the fractal was simulated with both sharp corners and corners rounded to a 23 nm radius. Material properties and film thickness were kept constant, while the applied magnetic field was set to zero and the transport current to 80 μ A to isolate geometric effects. The results are shown in Figure 15. It is evident that the sharp-corner layout exhibits stronger current crowding, which reduces the critical current and narrows the available bias margin, making it more difficult to reach saturation of the IDE.

To quantitatively assess the impact of corner rounding on current crowding, three metrics were used and interpreted as follows. K_0 represents the typical background current level in the less stressed regions, slightly higher values suggest a more uniform current distribution. $CI_{0.95}$ represents the height of the tail of the current distribution, corresponding to the 95th percentile and normalized to the reference level K_0 . A lower $CI_{0.95}$ indicates that fewer regions experience extremely high current densities. $A_{>1.3}$ is the fraction of the nanowire area where the local current exceeds $1.3 \cdot K_0$, so smaller values correspond to less extensive regions of high current concentration.

Corner Type	$CI_{0.95}$	$A_{>1.3}$	K_{0}
Rounded	1.7146	0.5473	1.476×10^{3}
Sharp	2.2056	0.7969	1.151×10^{3}

Table 2: Comparison of current crowding metrics for sharp and rounded corners.

The results, shown in Table 2 indicate that rounding the corners reduces both the peak crowding and the fraction of highly stressed regions, while leading to a more uniform current distribution. Consequently, the rounded design allows a higher critical current and more reliable SNSPD operation.

At this stage, it was necessary to evaluate how corner rounding affects optical performance, as the edges of the fractal act as excitation points for plasmonic modes [36]. Two optical simulations were performed, one with rounded corners and one with sharp corners. As shown in Figure 16, the reduction in absorption is not critical for device operation, with a decrease of approximately 5% within the spectral range of interest.

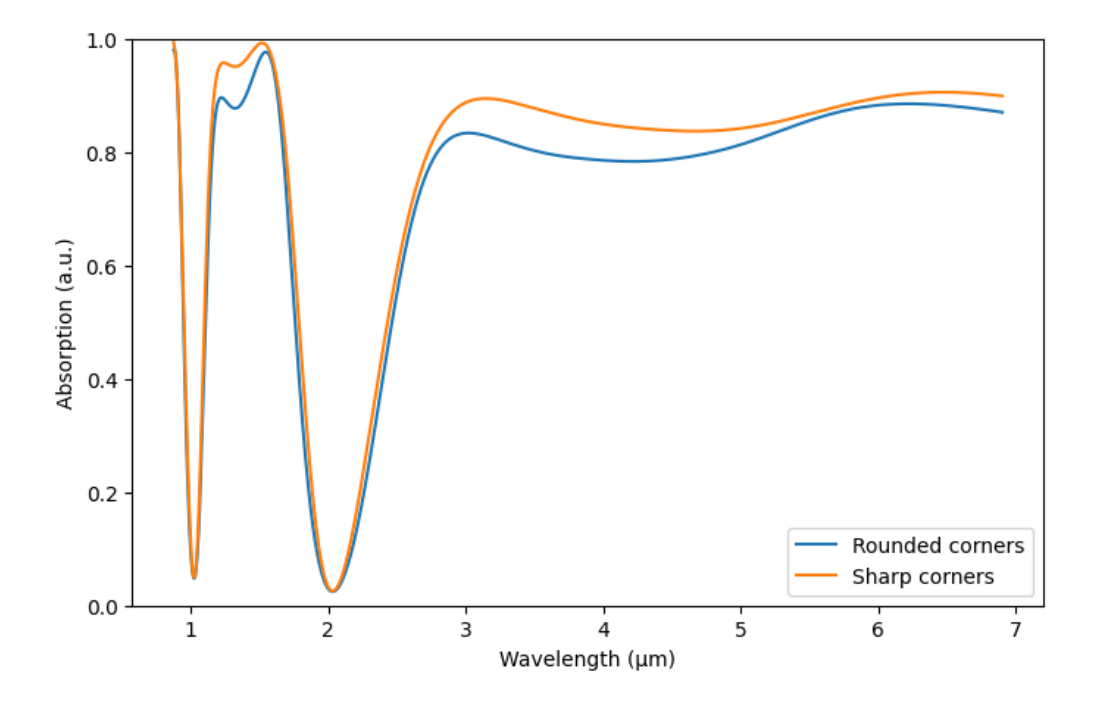


Figure 16: Impact of corner curvature on absorption spectrum, comparing structures with rounded and sharp corners.

Based on these results, the rounded-corner design was selected as the final structure, taking into account the trade-off between optical performance and the superconducting behavior required for a fully functional MIR SNSPD.

2.5.2 Absorption Efficiency and Performance Metrics

The final optimized structure is shown in Figure 17, with the selected parameters: a dielectric layer thickness of 1.35 μ m, a fractal thickness of 20 nm, a step length of 100 nm, and a nanowire width of 40 nm.

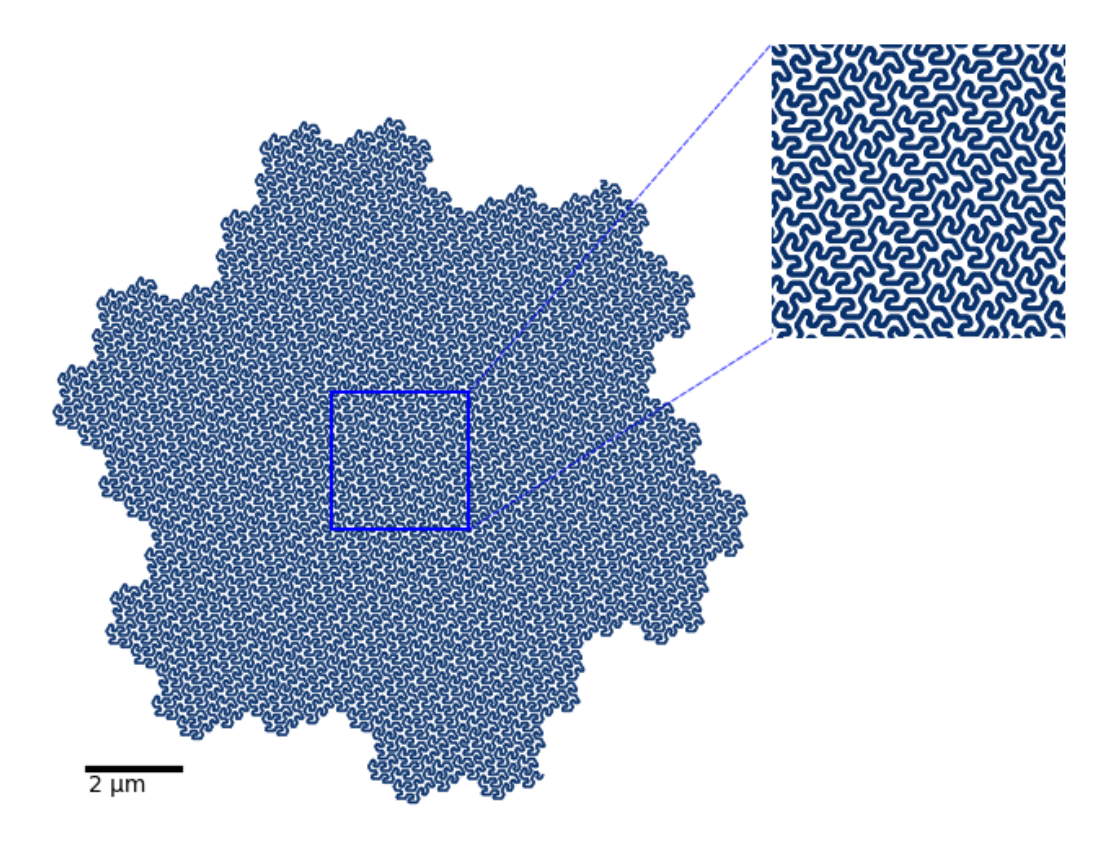


Figure 17: Final optimized fractal design, with final parameters: dielectric layer thickness of $1.35 \mu m$, fractal thickness of 20 nm, step length of 100 nm, and nanowire width of 40 nm.

The absorption, transmission, and reflection spectra of this configuration were then evaluated, as shown in Figure 18. The absorption spectrum exhibits broadband behavior within the 3–7 μ m range, with an average absorption of 82%.

Additionally, the polarization of the incident source was varied from TM, which is commonly used, to TE by rotating the polarization angle by 90 degrees. As illustrated in Figure 19, the absorption spectra for both polarizations are nearly identical. Quantitative analysis confirms this: the mean absolute difference over the 3–7 μ m range is 0.0135, the relative difference is 1.64%, and the correlation coefficient is 0.945. These results indicate that the structure is effectively polarization-insensitive across the MIR range, ensuring consistent performance for the intended application.

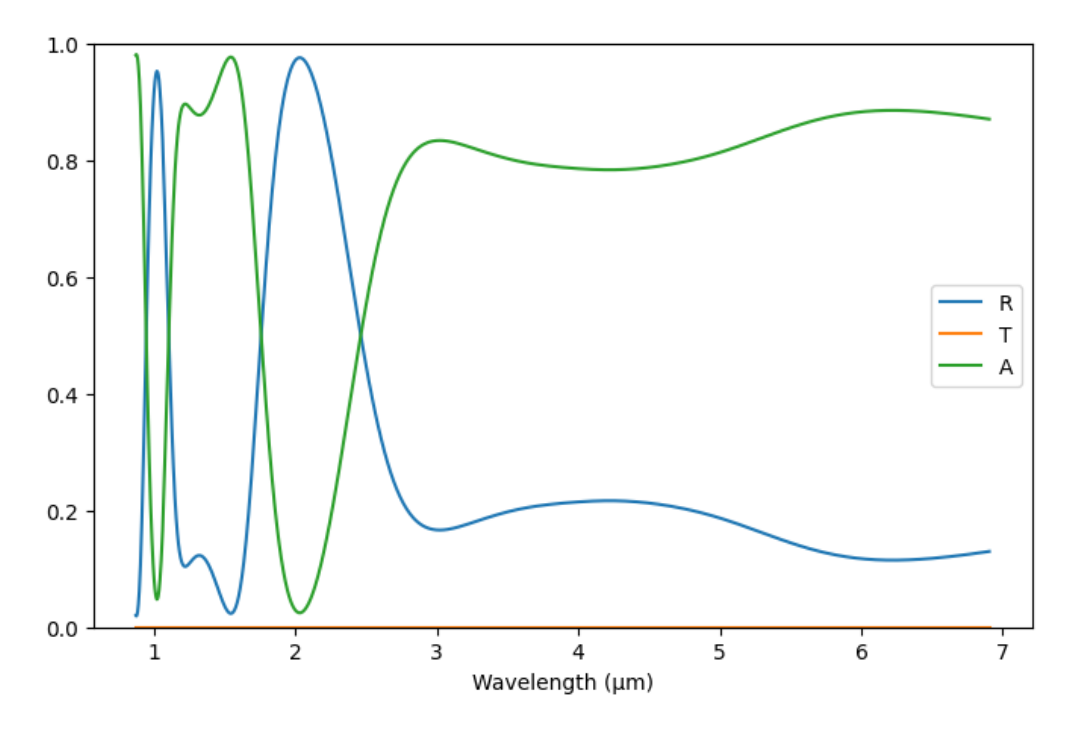


Figure 18: Absorption, reflection, and transmission spectra of the final optimized fractal design. The geometry was tuned to achieve high efficiency, broadband response, and fabrication feasibility.

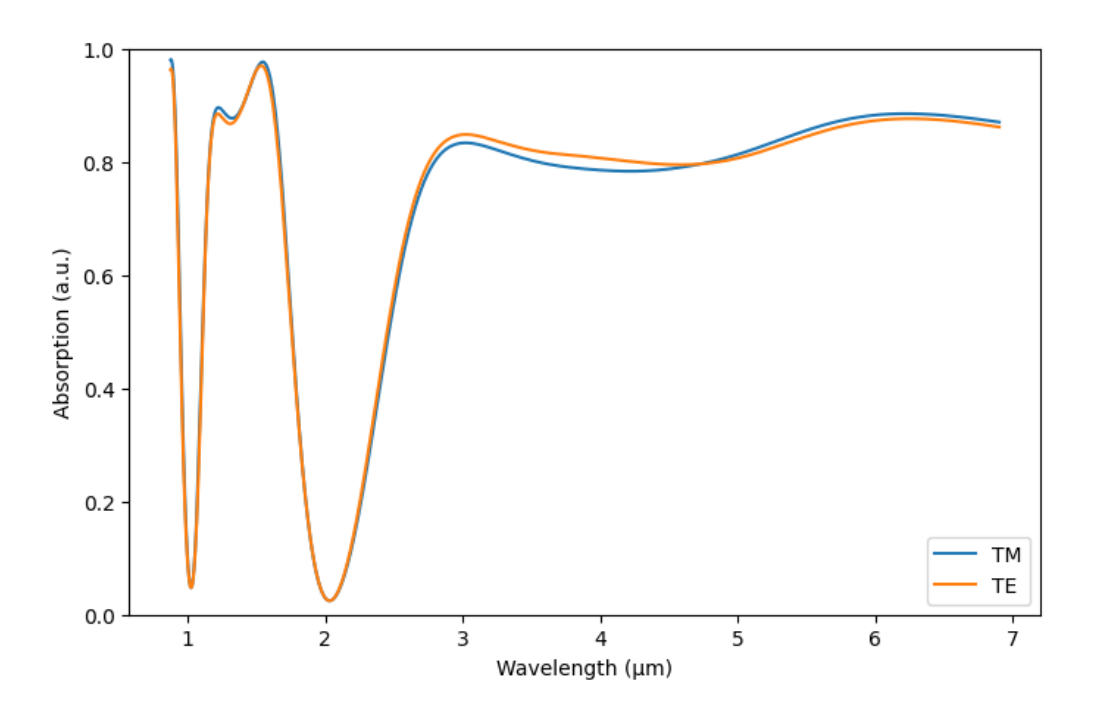


Figure 19: Comparison of absorption performance for TM and TE polarizations. The optimized structure exhibits polarization-insensitive behavior across the MIR spectrum, ensuring consistent detector performance.

The ability to maintain polarization insensitivity is a highly desirable property for SNSPDs, particularly in quantum information applications. In scenarios where the photon polarization is unknown, time-varying, or randomly distributed, aligning the polarization to maximize the detection efficiency of conventional meandered nanowire designs becomes challenging.

Fractal-based architectures have already been explored in the literature as a potential solution to this issue [45]. However, the design proposed in this work not only preserves polarization-independent behavior but also extends the operational range of the detector into the MIR region, achieving enhanced optical absorption.

In the following section, an experimental study is presented to demonstrate the feasibility of the proposed device through EBL and preliminary characterization. The lithography layout was generated using PHILD, a Python-based hierarchical layout design tool specifically developed for creating complex nanostructures with precise control over geometric parameters (Figure 20).

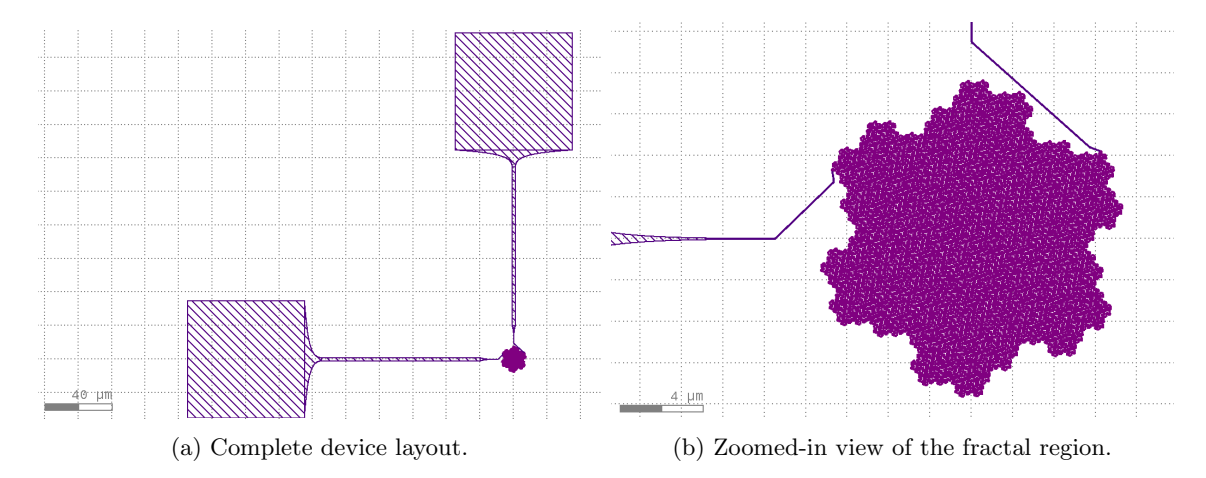


Figure 20: Layout design of the fabricated fractal SNSPD. (a) Full layout of the fabricated fractal SNSPD, showing the contact pads, hyperbolic tapers, nanowire section, and central fractal structure. (b) Magnified view of the fractal region highlighting the fine geometrical details generated with PHILD for EBL fabrication.

Metallic pads measuring 70 μ m × 70 μ m were connected to the fractal structure to enable electrical interfacing. These pads were linked to a 2 μ m-wide nanowire through hyperbolic tapers, which were again employed to connect the nanowire to the fractal region. This configuration ensured a smooth, linear transition between sections of the device, minimizing sharp bends that could induce current crowding and degrade superconducting performance.

3 Experimental Fabrication and Characterization

3.1 Nb Thin Film Deposition by Sputtering

The first step toward the experimental validation of the proposed structure involved the deposition and characterization of Nb, the material selected for the realization of the fractal design. Nb thin films were deposited using a magnetron sputtering technique, which provides precise control over film thickness, composition, and microstructure. Sputtering is a physical vapor deposition (PVD) process in which energetic ions from a plasma eject atoms from a solid target, which then condense onto a substrate to form a uniform coating. This method is widely used for superconducting materials such as Nb because it produces dense, adherent films with excellent reproducibility. In this work, an AJA magnetron sputtering system present in the Kostas Nanofabrication Laboratory at Northeastern University was employed, allowing independent adjustment of key parameters such as argon flow, sputtering current, process pressure, and substrate temperature. The system also enables control over the distance between the target and substrate, as well as the sputtering angle, providing flexibility to optimize film properties for superconducting applications.

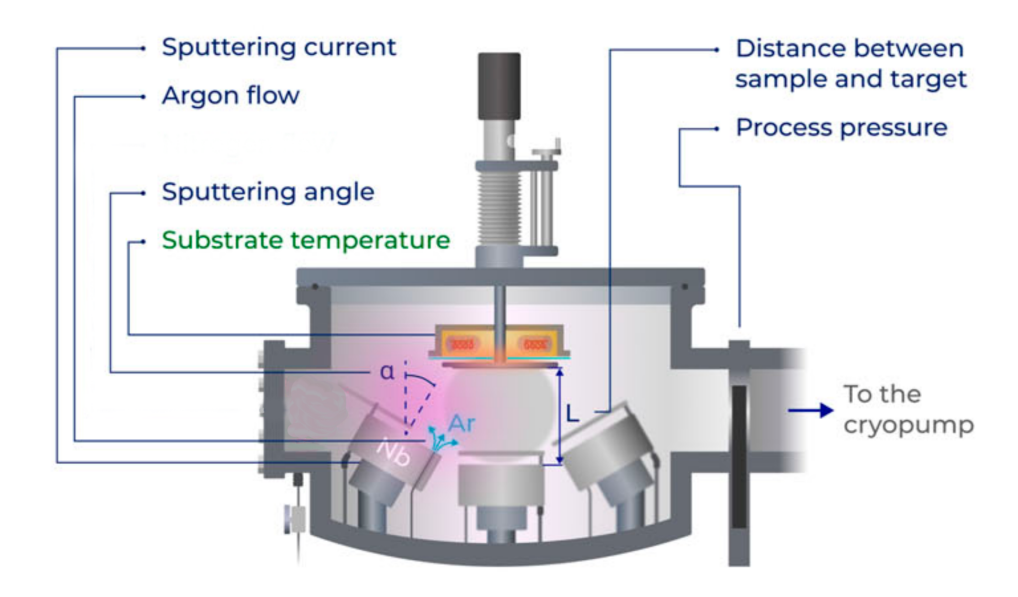


Figure 21: Schematic of the AJA magnetron sputtering chamber used for niobium thin-film deposition. The diagram highlights the main process parameters: sputtering current, argon gas flow, process pressure, target–substrate distance L, sputtering angle α , and substrate temperature. Argon plasma ions (Ar^+) bombard the Nb target, ejecting atoms that condense onto the heated substrate, while a cryopump maintains a high-vacuum environment. Adapted from [46]

Figure 21 ([46]) illustrates the main components and operating principles of the AJA sputtering chamber used in this study. The process takes place inside a high-vacuum chamber, where an inert argon (Ar) atmosphere is introduced at a controlled flow rate to sustain a plasma. A negative sputtering current is applied to the Nb target, generating Ar^+ ions that bombard the target surface and eject Nb atoms. These atoms travel through the chamber and condense onto the substrate, forming a uniform thin film. Key process parameters include the sputtering current, argon flow, process pressure, and the distance L between the target and substrate, which together govern the deposition rate and film quality. The substrate temperature is actively controlled to promote adhesion and tailor film properties, while the sputtering angle α can be adjusted to optimize thickness uniformity across the sample. A cryopump maintains the required base pressure by continuously evacuating residual gases, ensuring a clean environment for reproducible Nb deposition.

The depositions were carried out using fixed parameters and varying deposition times to enable a more comprehensive characterization of the sputtered material. The substrate was a 300 nm thick SiO_2 layer on Si. The wafer was diced into 1 cm \times 1 cm pieces to optimize the process without excessive costs and to ensure good conformality. The argon flow was set to 26.5 sccm, following values reported in the literature [47]. The DC current was fixed at 353 mA, based on previous optimized work performed by Lorenzo Barbati in the NSL group. Depositions were conducted at room temperature with a 45° sputtering angle and a 7 cm distance between the target and the sample.

To prevent oxidation of the Nb, which would degrade its superconducting properties, an in-situ Si capping layer was deposited immediately after the Nb film. The capping was performed using the Si target available in the AJA system with an RF bias . Its thickness was characterized on a SiO_2 substrate. Using a RF power of 120 W and a deposition time of 90 s the resulting thickness was 2 nm.

Three different deposition times (120 s, 180 s and 240 s) were tested to enable the characterization of sheet resistance, critical current, thickness and optical properties by ellipsometry.

3.2 Material Characterization

3.2.1 Sheet Resistance Measurements

The first characterization performed was the calculation of the sheet resistance of sputtered thin films, measured with a collinear four-point probe. The estimate is based on the ideal thin-film relation

$$R_{\square} = \frac{\pi}{\ln(2)} \cdot \frac{V}{I} \tag{4}$$

which holds when the film thickness is much smaller than the probe spacing and edge effects are negligible. In our setup the four tips are aligned and equally spaced on the sample surface. For this geometry we apply a corrective factor of 0.83 that accounts for the specific probe arrangement and deviations from the infinite sheet assumption. The values reported in the table 3 already include this correction.

Deposition time (s)	Sheet Resistance $(\frac{\Omega}{\Box})$
120	49.66
180	12.98
240	8.28

Table 3: Sheet resistance computed for different deposition durations.

Measurements were performed at room temperature using direct current, sourcing the current through the two outer probes and sensing the voltage between the two inner probes. Each data point represents the average between the horizontal and vertical measurements on the chip.

The results show that increasing the growth time lowers R_{\square} by roughly a factor of 6 between 120 s and 240 s. This trend is consistent with thickness increasing with time at an approximately constant sputter rate, since R_{\square} should scale inversely with thickness if the bulk resistivity remains constant. Any deviation from a simple $\frac{1}{t}$ behavior suggests that the intrinsic resistivity evolves with process time, likely due to microstructure changes such as grain growth, improved continuity, and reduced scattering from grain boundaries or voids that are common in early growth stages of sputtered Nb [48].

3.2.2 Critical Temperature Measurements

Measuring the critical temperature (T_c) is essential to evaluate the superconducting properties of the deposited Nb films. This parameter provides direct insight into the material's purity, homogeneity, and overall quality, as it reflects the transition from the normal to the superconducting state. In this study, T_c measurements were performed only on samples obtained with the shortest

(120 s) and the longest (240 s) deposition times, as these represent the two extremes of the process window.

3.2.2.1 Cryogenic Setup

The T_c of the Nb films was measured using a custom-built compact cryogenic probe station designed by Liam Kelly and implemented with the collaboration of the entire NSL lab. (Figure 22).

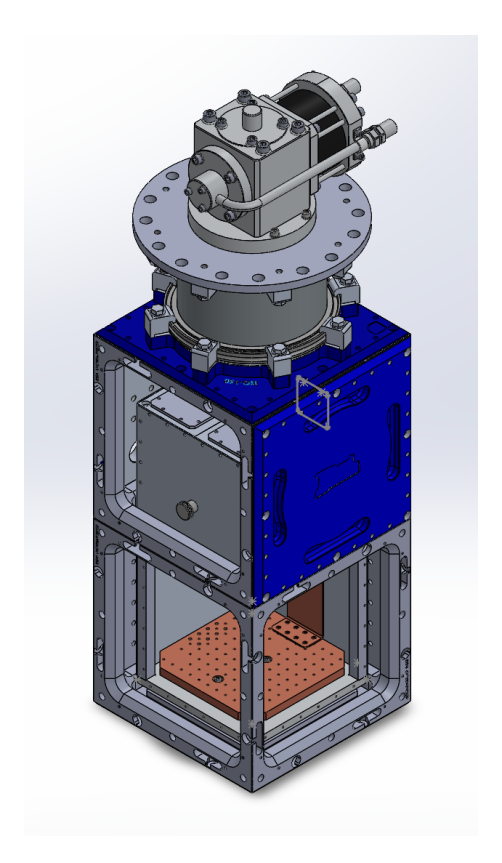


Figure 22: 3D Computer-Aided Design (CAD) of the cryostat for T_c measurements.

The system consists of a modular vacuum chamber with integrated closed-cycle cryogenic cooling, providing both mechanical stability and high thermal conductivity. The sample is mounted on a copper cold plate, which is thermally anchored to the cryocooler, and includes a resistive heater and calibrated thermometers for precise temperature control. Electrical connections are routed through multi-pin vacuum feedthroughs, enabling four-point measurements with low-noise twisted wires. A source-meter applies the current, while a nanovoltmeter records the voltage drop. Temperature sweeps are controlled via a dedicated temperature controller, allowing slow and reproducible ramps across the superconducting transition. This setup permits accurate R(T) measurements of Nb films, ensuring reliable determination of T_c within the 4–20 K range.

3.2.2.2 Results

Figure 23 shows the resistance as a function of temperature for the Nb film deposited for 120 s. To determine the T_c , the data were analyzed using the standard 10–90 % criterion: the temperatures corresponding to 90 % and 10 % of the normal-state resistance were identified, and their average was taken as T_c . Using this method, a critical temperature of

$$T_C = \frac{T_C(90\%) + T_C(10\%)}{2} = \frac{5.27K + 5.14K}{2} = 5.20K$$

was obtained.

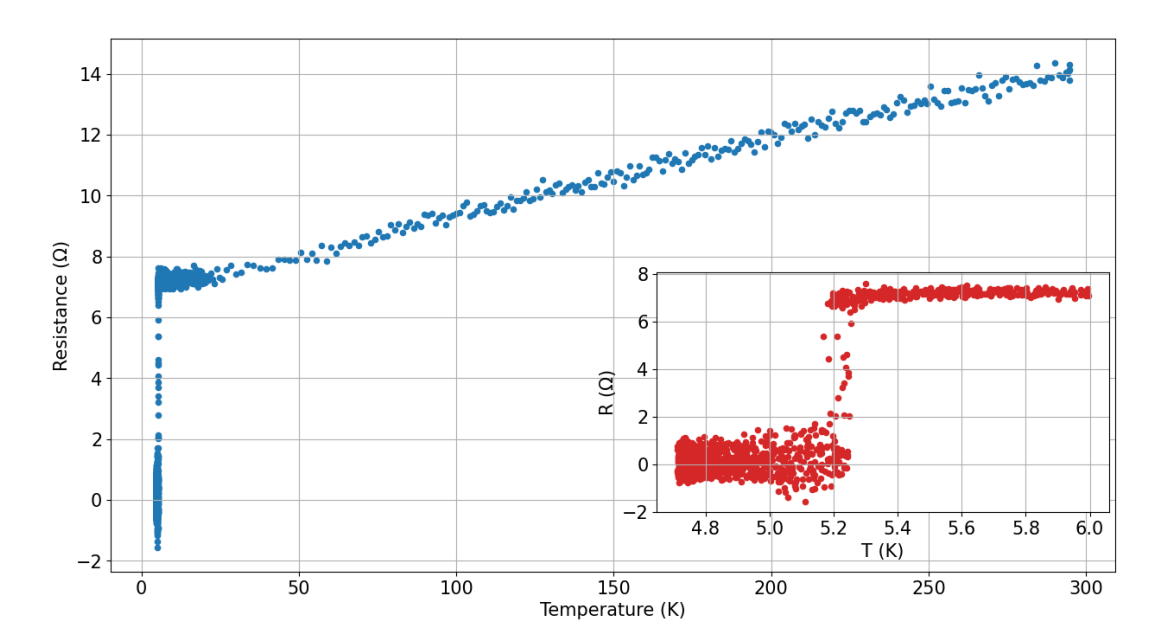


Figure 23: Resistance vs. temperature curve for the Nb sample sputtered for 120 s. The inset provides a zoomed view of the superconducting transition.

From the same measurement, the residual resistivity ratio (RRR) was calculated as the ratio between the resistance at room temperature and the resistance just above the transition.

$$RRR = \frac{R_{RT}}{R_{20K}} = 1.87$$

The RRR provides information about the material's purity and structural order; the value measured here is consistent with reports in the literature for Nb thin films of similar thickness [49].

For the film deposited for 240 s, the resistance data reveal a clear superconducting transition at

$$T_C = \frac{T_C(90\%) + T_C(10\%)}{2} = \frac{7.02K + 6.82K}{2} = 6.92K.$$

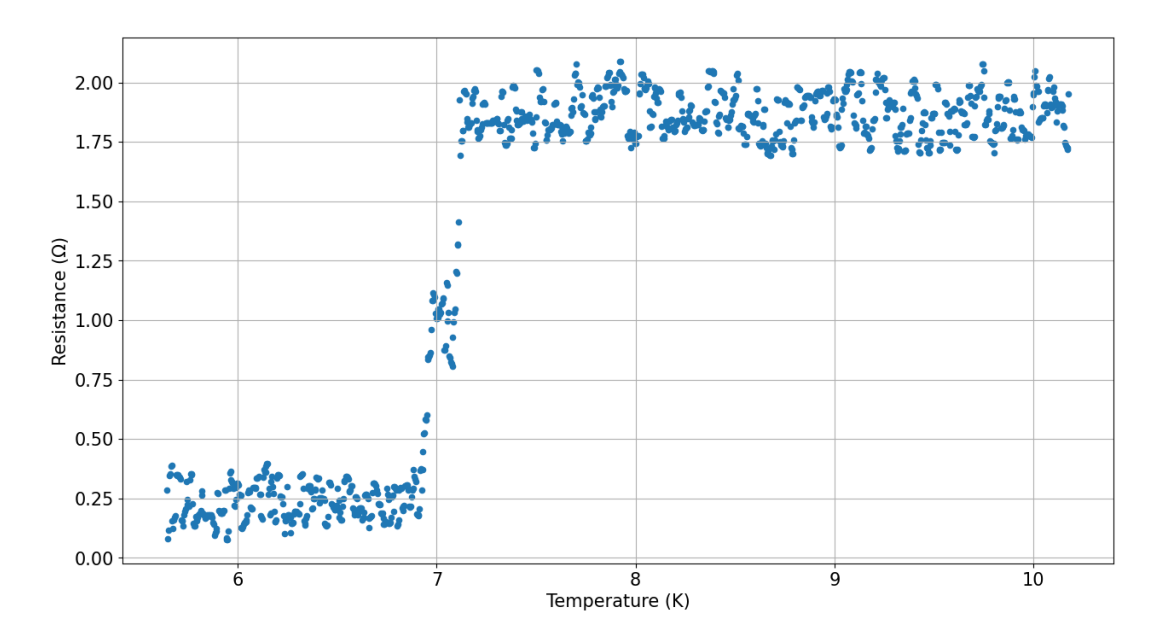


Figure 24: Resistance vs. temperature curve for the Nb sample sputtered for 240 s.

The higher T_c compared with the thinner sample is likely related to the increased thickness of the film, which can promote better crystalline order and reduce scattering from surface or grain-boundary defects. In thicker films, the influence of surface oxidation and interface roughness is reduced, and the material can approach the bulk-like regime where superconductivity is less suppressed by disorder and finite-size effects. These observations confirm the expected improvement of superconducting properties as the film thickness increases [48].

3.2.3 Ellipsometry Measurements

Optical characterization of the films was performed using a Semilab SE2000 ellipsometer at MIT.nano. Ellipsometry is a non-destructive technique that measures the change in polarization of light upon reflection from a sample surface; from these data, the complex refractive index (n, k) and the thickness of thin films can be extracted. Measurements were acquired at three incidence angles $(75^{\circ}, 70^{\circ}, \text{ and } 65^{\circ})$ to increase sensitivity and improve the robustness of the fit.

For materials whose optical properties are not tabulated, it is necessary to construct a physical model that links the optical constants and the film thickness. The availability of samples with different deposition times provided an additional constraint, allowing the thickness to be treated as a known parameter and reducing the number of free variables in the fitting procedure. Two complementary algorithms were employed: Price's algorithm, used as a global optimizer, and the Levenberg–Marquardt algorithm (LMA), used for local refinement of the solution. The goal was to find a consistent set of refractive index (n) and extinction coefficient (k) values that could simultaneously fit all the data across different thicknesses.

A combined Drude–Lorentz model was adopted to describe the optical response of Nb, shown in Figure 25, yielding optical constants in close agreement with tabulated values [43]. The goodness of fit was quantified by the coefficient of determination (R^2) . For the three Nb films of different thicknesses, the simultaneous fit achieved $R^2 = 0.914$ (120 s), 0.9675 (180 s), and 0.9427 (240 s), indicating consistently good agreement across all samples.

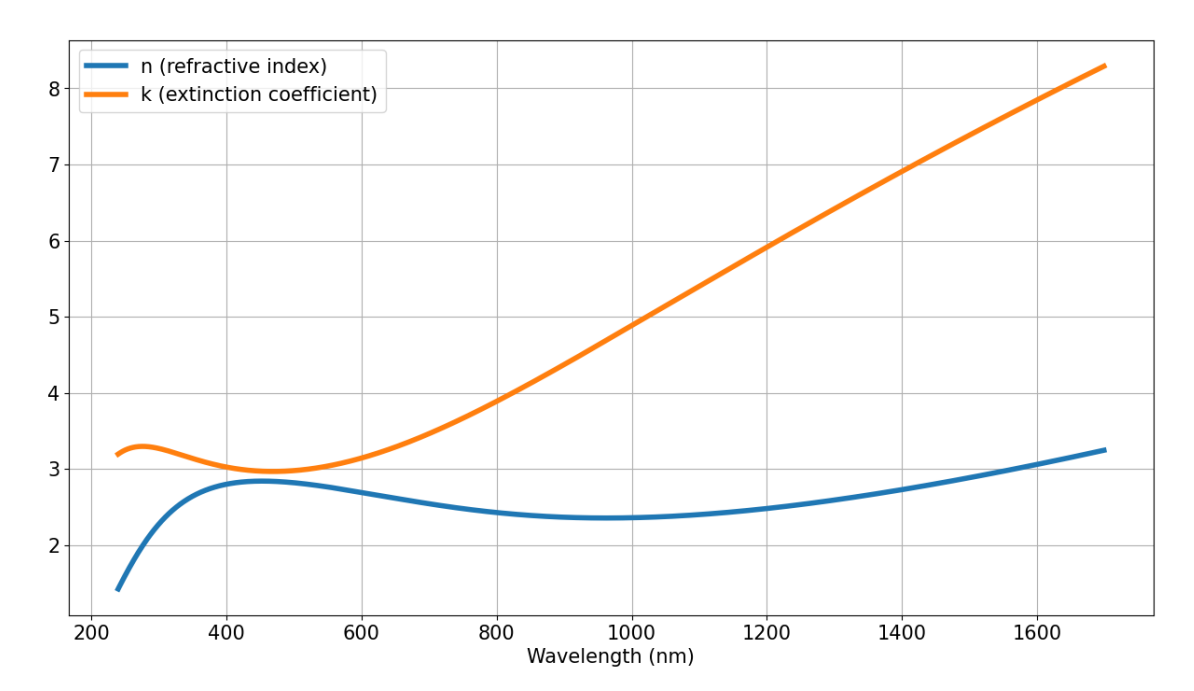


Figure 25: Optical properties (refractive index and extinction coefficient) as functions of wavelength extracted from ellipsometry measurements.

Once the optical model was established, the film thicknesses for the various deposition times were determined, as shown in the table 4, revealing a clear linear relationship between thickness and deposition time, as expected for a uniform sputtering process (Figure 26).

Deposition time (s)	Thickness (nm)
120	10.6
180	14.8
240	19.2

Table 4: Thickness measured for different deposition durations.

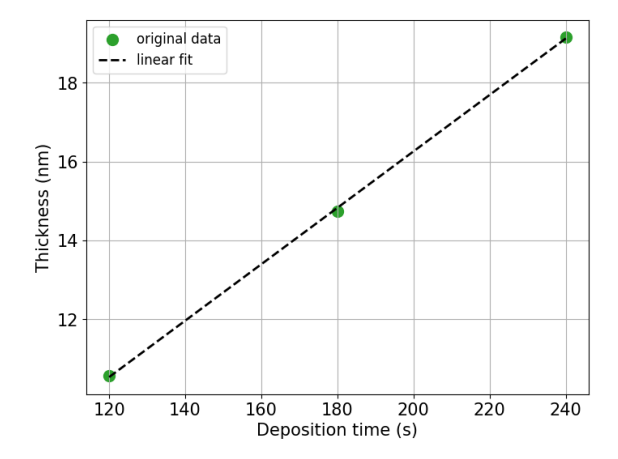


Figure 26: Ellipsometry-derived thickness vs. deposition time with linear fit, consistent with a constant deposition rate.

3.3 Device Fabrication Process

The following objective was to fabricate the superconducting Nb fractal structures with minimum linewidths of 40 nm on a $\rm SiO_2/Au$ stack and, for the final device, to encapsulate the metal with a silica-like dielectric layer. Because the optical performance depends critically on the fidelity of the smallest features and on clean pattern transfer into Nb, a dedicated lithography-development stage was executed prior to the full flow.

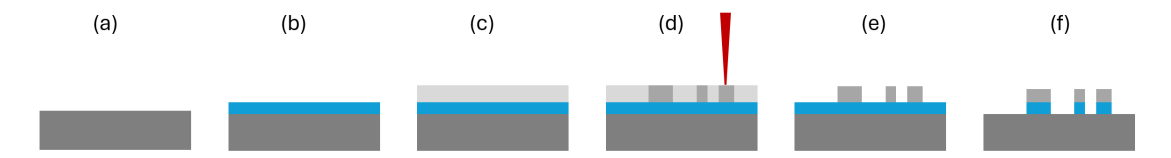


Figure 27: Preliminary simplified process for Nb patterning on SiO₂. (a) SiO₂ on substrate. (b) Sputtered Nb thin film. (c) Spin-coat negative e-beam resist. (d) E-beam exposure to write the pattern. (e) Resist development. (f) Nb RIE etching to form the Nb features.

A short, optimization-oriented process was first established to decouple lithography and etch from the rest of the stack, shown in Figure 27. Nb was deposited on SiO₂, a negative e-beam resist was spun, the fractal layout was exposed and developed, and the Nb was etched using the cross-linked resist as a hard mask. Electron-beam lithography was carried out at MIT.nano on the Elionix ELS-HS50 (50 kV vector-scan system with electrostatic beam blanking). Before writing the fractal, proximity effect correction (PEC) was applied to achieve more accurate definition of the structure's fine features.

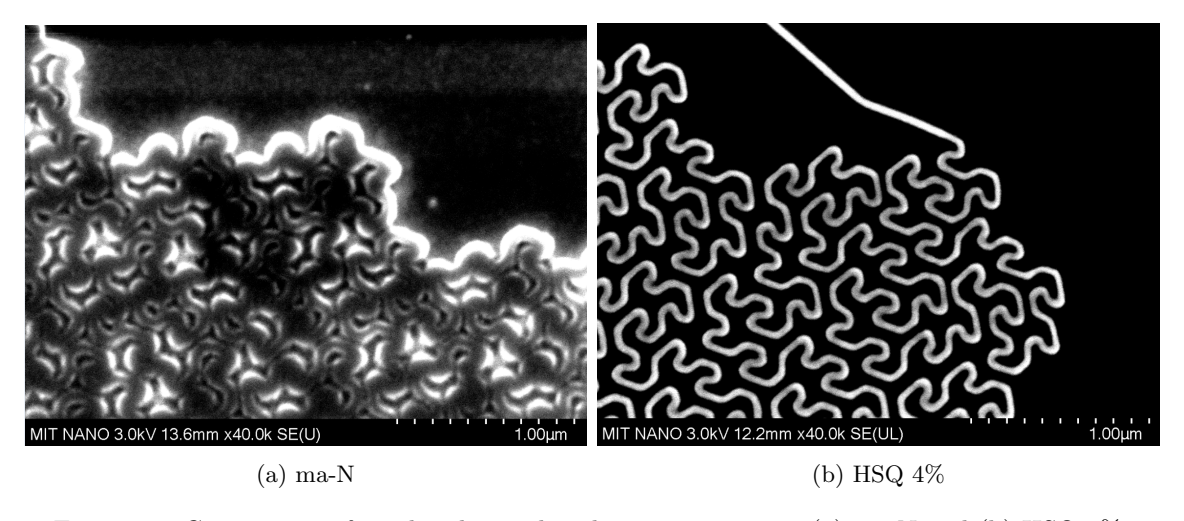
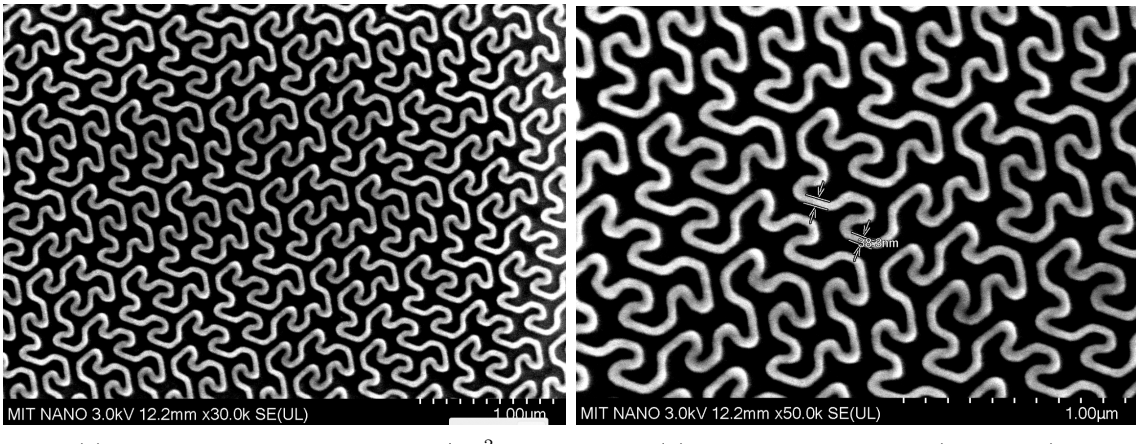


Figure 28: Comparison of results obtained with negative resists: (a) ma-N and (b) HSQ 4%.

Two negative resists were screened: ma-N 2401 series negative e-beam resist (ma-N) and hydrogen silsesquioxane (HSQ) 4%. Comparative scanning electron microscopy (SEM) images (Figure 28) show that ma-N did not reach the target 40 nm linewidths with adequate fidelity. HSQ, by contrast, consistently produced features at the required dimension with uniform edges and good line continuity, and was therefore selected for the subsequent steps. Dose calibration was then performed while keeping the writing current (1 nA) and development chemistry fixed (Tetramethylammonium hydroxide 25%, 90 s). The optimal area dose for the fractal motifs was $1300~\mu\text{C}~\text{cm}^{-2}$, as confirmed by SEM (Figure 29). A layout peculiarity is the set of narrow, isolated connectors linking the contact pads to the fractal; these segments exhibited delamination when written at reduced dose (Figure 30a). To ensure mechanical integrity, the connectors were written at a fixed higher dose of 2000 $\mu\text{C}~\text{cm}^{-2}$ (Figure 30b). All SEM images were acquired at MIT.nano using a Hitachi Regulus 8100 scanning electron microscope operated at an accelerating voltage of



(a) HSQ structure, dose: $1300 \ \mu\text{C/cm}^2$

(b) Zoom on the features ($\sim 38.3 \text{ nm}$)

Figure 29: Example of high-quality HSQ fabrication. (a) Structure obtained at a dose of $1300~\mu\text{C/cm}^2$, showing excellent pattern definition. (b) Magnified view of the lines, with a measured feature width of ~ 38.3 nm, close to the 40 nm design target.

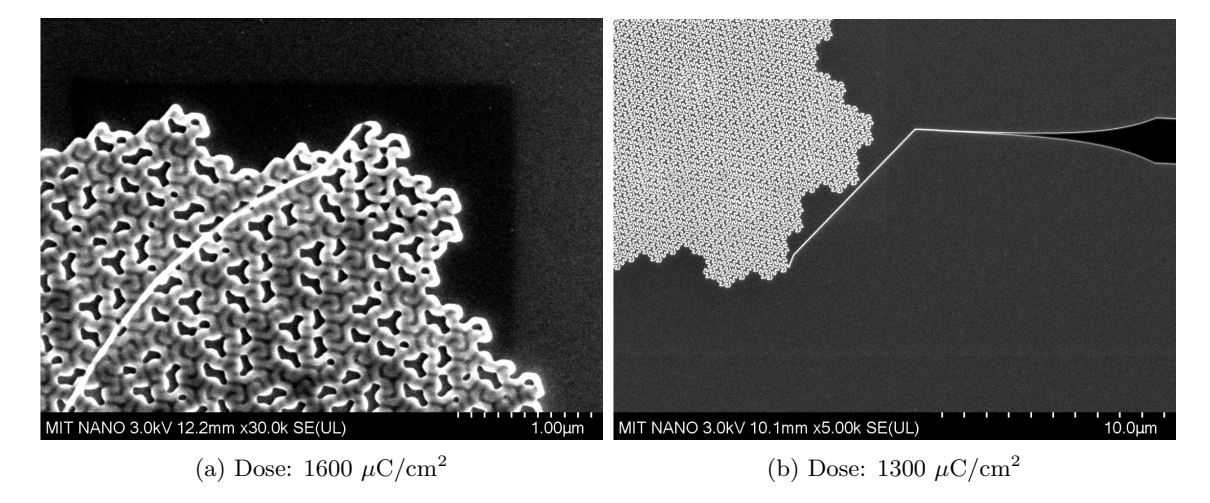


Figure 30: Comparison of HSQ exposure results. (a) At a dose of 1600 μ C/cm², delamination is visible in the connector region. (b) At a lower dose of 1300 μ C/cm², the pattern remains intact; the delamination issue was solved by increasing the connector dose to 2000 μ C/cm².

Pattern transfer into Nb was executed in the Northeastern clean room on a PlasmaTherm 790 reactive ion etching (RIE). In this configuration the inductively coupled coil (RF2) sustains a high-density plasma and controls ion flux, while the biased platen (RF1) sets ion energy for anisotropic etching. HSQ behaves as a silica-like hard mask with strong selectivity in fluorine chemistry. Etching with SF₆ at 30 sccm, RF1 = 20 W (bias) and RF2 = 100 W (inductive power) yielded faithful transfer of the 40 nm features.

With lithography and etch validated, the complete device process was proposed (Figure 31). Starting from a Si substrate with a sputtered Au ground plane, a conformal SiO_2 layer is then deposited using plasma-enhanced chemical vapor deposition (PECVD) technique. After the sputtering of Nb, HSQ 4% is spun, exposed with the fractal pattern, developed, and used as the hard mask for Nb etching. An HSQ FOx-16 over-coat is then applied to bury the metal features and to reach the target SiO_2 -equivalent top-layer thickness. A second e-beam exposure cross-links the over-coat, followed by a thermal cure that densifies HSQ into a silica-like over-cladding, thereby providing the required dielectric layer.

A variation of this fabrication process was developed to obtain a device suitable for optical measurements using Fourier-transform infrared (FTIR) spectroscopy (Section 3.4.3). Since this type of spectroscopy uses an illumination spot significantly larger than the dimensions of the standard device, a larger fractal structure was fabricated to reproduce the "infinite fractal" effect assumed in the simulations, where a 5 μ m spot size was used. For this purpose, a stage-7 fractal with overall dimensions of 100 μ m × 100 μ m was designed and fabricated.

The patterning was performed using PEC, and the exposure dose was reduced to $800 \ \mu\text{C/cm}^2$ to achieve the desired resolution. After the etching step, because maintaining the superconducting properties of Nb was not essential for this optical characterization, a SiO_2 layer was deposited by PECVD. This deposition method is generally avoided for layers below superconducting devices, as the substrate heating required during the process can degrade the superconducting performance of Nb.

This specific device was therefore fabricated exclusively for optical measurements.

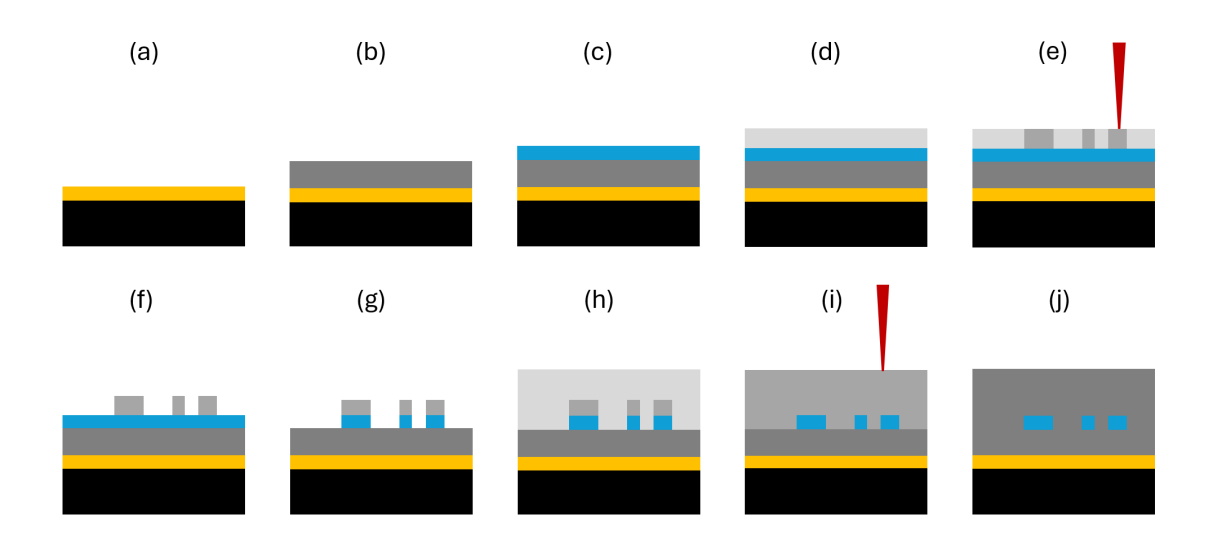


Figure 31: Complete fabrication process for the device. (a) Si substrate with sputtered Au ground plane. (b) Conformal SiO_2 dielectric deposited on Au. (c) Sputtered Nb thin film. (d) Spin-coat negative e-beam resist. (e) E-beam exposure to write the Nb pattern. (f) Resist development. (g) Nb RIE etching to form the Nb features. (h) HSQ FOX16 over-coat. (i) E-beam exposure of the HSQ over-coat to cross-link and harden. (j) Post-exposure bake to densify the HSQ into a silica-like (SiO_2) layer.

3.4 Preliminary Device Performance Characterization

Once the device fabrication was completed, two characterizations were performed: first, an electrical characterization in the cryogenic setup, and second, an optical characterization using FTIR spectroscopy.

3.4.1 Cryogenic Setup

The cryogenic measurements were conducted using a commercial DRY ICE 1.0K system from ICEoxford, featuring a three-stage cooling configuration. This cryostat uses a closed-cycle pulse-tube refrigerator, eliminating the need for liquid cryogens. The system achieves base temperatures down to 1 K. The three-stage cooling process involves progressive thermal isolation: the first stage operates at 50 K, the second at 4 K, and the third at 1 K. This design ensures efficient heat dissipation and minimizes mechanical vibrations. Electrical access to the sample was facilitated through low-noise coaxial wiring, enabling precise I–V and switching current measurements under controlled cryogenic conditions.

The circuit used for the I–V measurements is designed to provide a controlled current to the device while accurately monitoring the voltage drop (Figure 32).

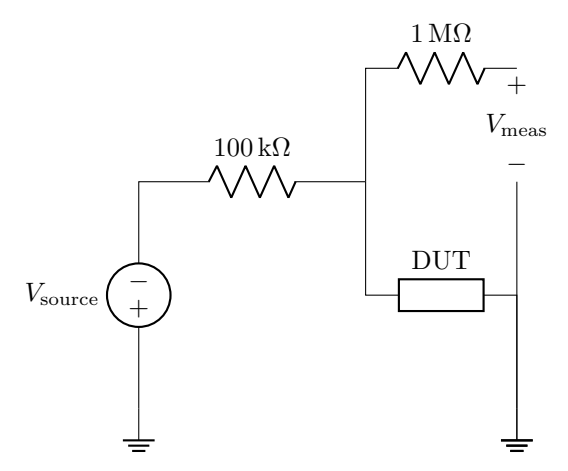


Figure 32: Schematic of the I–V measurement circuit. A voltage source in series with a 100 k Ω resistor provides a quasi-constant current to the DUT inside the cryostat. A T-junction splits the connection between the device and the multimeter, with a 1 M Ω resistor inserted in series to reduce noise.

A commercial Keysight B2901BL voltage source is connected in series with a fixed 100 k Ω resistor, which acts to limit the current and approximate a constant-current source for the device under test (DUT). A T-junction then splits the connection, with one branch leading to the DUT inside the cryostat and the other to a commercial Keysight 34465A multimeter for voltage measurement. To minimize electrical noise and improve measurement stability, a 1 M Ω resistor is added in series at the multimeter input. This configuration allows precise characterization of the I–V response while protecting the device and the measurement instruments.

3.4.2 Electrical Characterization

The devices tested in the cryogenic setup were those fabricated on ${\rm SiO_2/Si}$ substrates. A preliminary electrical characterization was performed to analyze the behavior of the critical current and to extract useful information for the subsequent characterization of the final device fabricated on the gold-based stack. The devices were mounted on a PSB (Printed Sample Board) designed by Faith Degawa (NSL Lab) and wire-bonded using aluminum. The measurements were performed at 1.6 K.

To investigate the influence of geometry on the I–V characteristics, a straight nanowire was fabricated and tested between two pads, with a thickness of 40 nm. The resulting I–V curve for this first device is shown in Figure 33. Interestingly, the nanowire exhibits a hysteretic behavior. This effect can be attributed to the fact that, at 40 nm, the film thickness is close to the coherence length of Nb, leading to slight inhomogeneities in the superconducting properties along the wire.

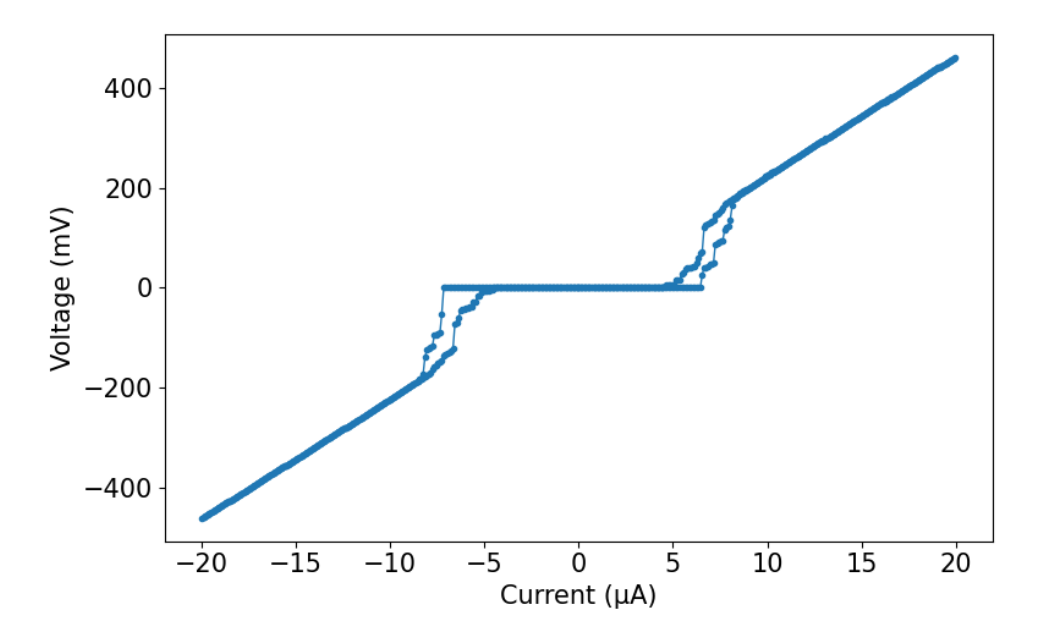


Figure 33: I–V characteristics of the 40 nm-wide nanowire device measured at 1.6 K. The nanowire serves as a preliminary test structure for evaluating variations in the I_c .

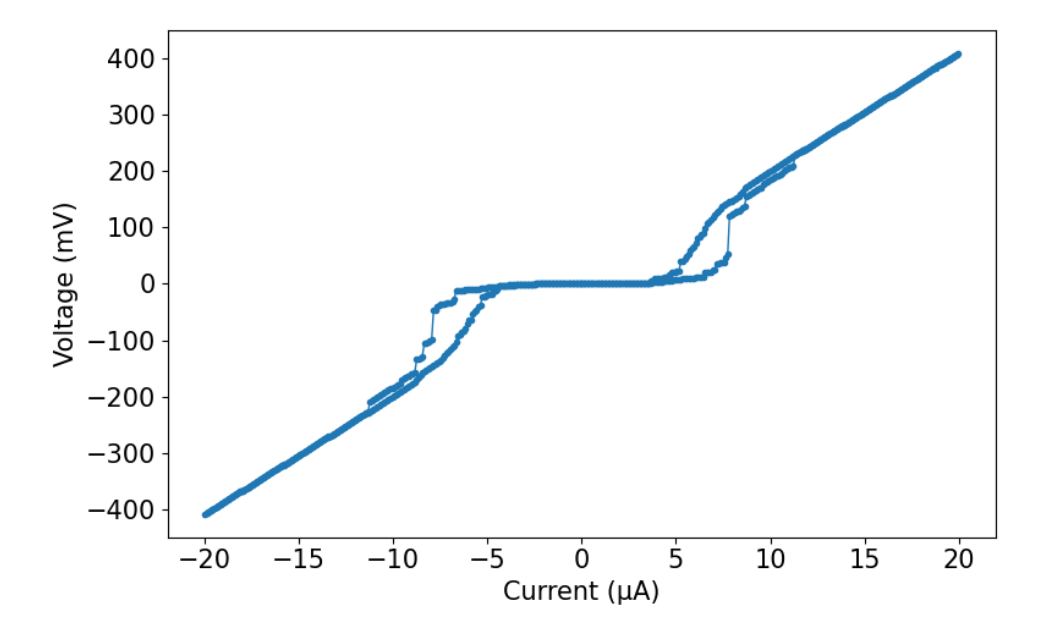


Figure 34: I–V characteristics of the fractal-shaped device measured at 1.6 K. The data show the critical current behavior of the fractal geometry.

Figure 34 shows the I–V curve for the fractal structure. It can be immediately observed that the transition, while still hysteretic, appears significantly smoother compared to the straight nanowire. This behavior is likely due to the complexity of the geometry: different regions of the

fractal switch at slightly different current values, resulting in a gradual transition rather than an abrupt jump. Moreover, the minimal variation observed in the critical current between the I–V characteristics of the nanowire and the fractal structure indicates that the fabrication process preserved the intrinsic superconducting properties of the material, with no evident degradation induced by patterning or processing steps.

3.4.3 Optical Characterization Using FTIR Spectroscopy

An optical characterization was performed using FTIR spectroscopy in collaboration with Aurelio Venditti (NanoSI at Northeastern University), which allows extracting the absorption spectrum of a structure within the MIR range. The FTIR technique operates by measuring the interference pattern generated when a broadband infrared beam is split, reflected by the sample, and recombined; from this interference signal, the spectral response of the device is obtained through a Fourier transform.

The measurement was carried out in the 1–7 μ m wavelength range to enable a direct comparison with the simulation results. The absorption spectrum obtained is shown in Figure 35.

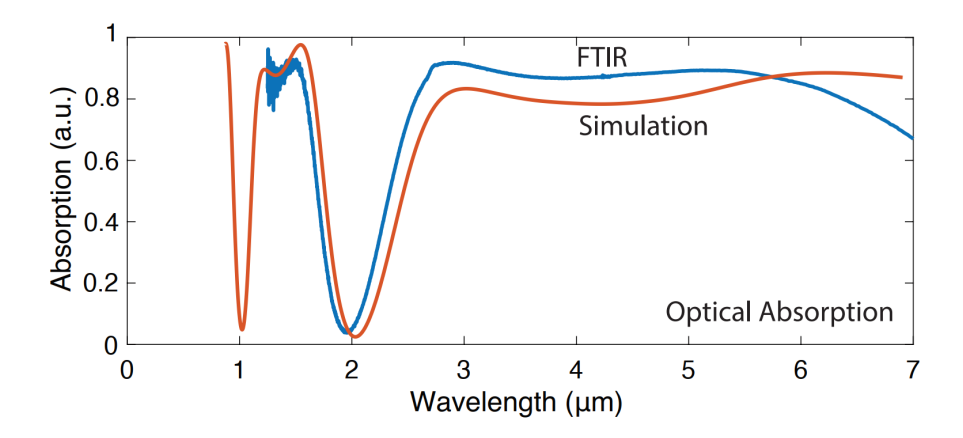


Figure 35: Comparison between simulated and experimental FTIR absorption spectra of the fabricated structures.

The results show good agreement between simulation and measurement. The slight shift of the absorption minimum compared to the simulations, as well as the gradual decrease in absorption beyond 6 μ m, is likely due to the dielectric layer being slightly thinner than expected. Indeed, as observed in the simulations presented in the previous section 2.5.1, reducing the SiO₂ thickness shifts the entire spectrum toward shorter wavelengths and reduces the broadband nature of the response. Nevertheless, these measurements confirm that the fabricated device closely matches the behavior predicted by the theoretical and simulated design.

4 Conclusions and Outlook

4.1 Summary of Main Results

The goal of this work was to propose an architecture for an SNSPD capable of operating in the MIR range, overcoming the limitations arising from the lack of compact methods to enhance optical absorption and, consequently, the detector's SDE in this spectral region.

In the development of this thesis, a structure was designed that combines the impedance-matching principle of a perfect absorber with a fractal geometry able to excite plasmonic modes at the target wavelengths identified between 3 and 7 μ m. The main structural parameters were optimized, with the most promising results obtained for a dielectric thickness of 1.35 μ m, a fractal thickness of 20 nm, and a fractal step length of 100 nm. These parameters were chosen by carefully balancing the trade-offs between optical absorption and the superconducting properties required for proper SNSPD operation. Simulations demonstrated an average absorption of 82% within the target range and a polarization-insensitive response, which is particularly beneficial for quantum information applications.

The experimental feasibility of the device fabrication was also validated by optimizing the deposition recipe for Nb and refining the EBL lithography process. An initial electrical characterization was carried out through I–V curve measurements, followed by an experimental verification of the optical simulated results via FTIR absorption spectroscopy.

These results confirm the feasibility of the proposed design and pave the way for its future implementation. This work represents an initial demonstration toward a new generation of SNSPDs capable of operating in the MIR with absorption efficiencies comparable to state-of-the-art performance in the NIR. The proposed plasmonically engineered approach offers a flexible framework that can be scaled, adapted, or integrated into practical detector architectures. Further optimization of materials and fabrication techniques will be essential to fully translate these concepts into scalable and reliable detector arrays.

4.2 Suggested Future Work

The next steps of this work will focus on demonstrating the full operation of the proposed device as an SNSPD. The first goal will be to build a dedicated cryogenic setup that allows testing of the detector performance, integrating a laser source and an oscilloscope to evaluate key metrics such as detection efficiency, timing jitter, and count rate.

In parallel, the development of a MIR source to be integrated into the cryostat will be pursued, enabling direct testing of the detector in the target wavelength range. The design and component selection for this MIR source have already been completed, and its implementation will represent a crucial step toward validating the detector's operation in the mid-infrared.

Finally, the fabrication of a fully functional device following the process flow proposed in this thesis will be carried out, allowing for a complete experimental validation of the plasmonically engineered SNSPD architecture.

The successful implementation of this architecture could open new possibilities for applications in MIR spectroscopy, free-space communication, and quantum sensing, where compact and efficient single-photon detectors are still lacking.

References

- [1] Iman Esmaeil Zadeh et al. "Superconducting nanowire single-photon detectors: A perspective on evolution, state-of-the-art, future developments, and applications". en. In: *Appl. Phys. Lett.* 118.19 (May 2021), p. 190502.
- [2] Ioana Craiciu et al. "High-speed detection of 1550 nm single photons with superconducting nanowire detectors". en. In: *Optica* 10.2 (Feb. 2023), p. 183.
- [3] Lixing You. "Superconducting nanowire single-photon detectors for quantum information". en. In: *Nanophotonics* 9.9 (July 2020), pp. 2673–2692.
- [4] Jiu-Peng Chen et al. "Sending-or-not-sending with independent lasers: Secure twin-field quantum key distribution over 509 km". en. In: *Phys. Rev. Lett.* 124.7 (Feb. 2020), p. 070501.
- [5] Hiroyuki Shibata, Toshimori Honjo, and Kaoru Shimizu. "Quantum key distribution over a 72 dB channel loss using ultralow dark count superconducting single-photon detectors". en. In: Opt. Lett. 39.17 (Sept. 2014), pp. 5078–5081.
- [6] Fabian Beutel et al. "Detector-integrated on-chip QKD receiver for GHz clock rates". en. In: Npj Quantum Inf. 7.1 (Feb. 2021).
- [7] Vidur Raj et al. "Waveguide integrated superconducting nanowire single-photon detectors for integrated photonics". In: J. Phys. D Appl. Phys. 58.24 (June 2025), p. 243001.
- [8] Emma E Wollman et al. "SNSPD-based detector system for NASA's Deep Space Optical Communications project". en. In: Opt. Express 32.27 (Dec. 2024), pp. 48185–48198.
- [9] Aongus McCarthy et al. "Kilometer-range, high resolution depth imaging via 1560 nm wavelength single-photon detection". en. In: *Opt. Express* 21.7 (Apr. 2013), pp. 8904–8915.
- [10] Li Chen et al. "Ultra-sensitive mid-infrared emission spectrometer with sub-ns temporal resolution". en. In: *Opt. Express* 26.12 (June 2018), pp. 14859–14868.
- [11] Amr Tamimi et al. "Deep mouse brain two-photon near-infrared fluorescence imaging using a superconducting nanowire single-photon detector array". en. In: ACS Photonics 11.10 (Oct. 2024), pp. 3960–3971.
- [12] Emma E Wollman et al. "Recent advances in superconducting nanowire single-photon detector technology for exoplanet transit spectroscopy in the mid-infrared". In: *J. Astron. Telesc. Instrum. Syst.* 7.01 (Jan. 2021).
- [13] G N Gol'tsman et al. "Picosecond superconducting single-photon optical detector". en. In: *Appl. Phys. Lett.* 79.6 (Aug. 2001), pp. 705–707.
- [14] Chandra M Natarajan, Michael G Tanner, and Robert H Hadfield. "Superconducting nanowire single-photon detectors: physics and applications". In: *Supercond. Sci. Technol.* 25.6 (June 2012), p. 063001.
- [15] Francesco P Venza and Marco Colangelo. "Research trends in single-photon detectors based on superconducting wires". en. In: *APL Photonics* 10.4 (Apr. 2025).
- [16] A Engel et al. "Detection mechanism of superconducting nanowire single-photon detectors". In: Supercond. Sci. Technol. 28.11 (Nov. 2015), p. 114003.
- [17] Andrew J Kerman et al. "Kinetic-inductance-limited reset time of superconducting nanowire photon counters". en. In: *Appl. Phys. Lett.* 88.11 (Mar. 2006), p. 111116.
- [18] Hui Wang et al. "Controlling the recovery time of the superconducting nanowire single photon detector using a tunable resistor". In: 2023 Conference on Lasers and Electro-Optics Europe & European Quantum Electronics Conference (CLEO/Europe-EQEC). Vol. 17. IEEE, June 2023, pp. 1–1.
- [19] J Chang et al. "Detecting telecom single photons with 99.52.07+0.5% system detection efficiency and high time resolution". en. In: APL Photonics 6.3 (Mar. 2021), p. 036114.
- [20] Jeff Chiles et al. "New Constraints on Dark Photon Dark Matter with Superconducting Nanowire Detectors in an Optical Haloscope". In: Phys. Rev. Lett. 128 (23 June 2022), p. 231802. DOI: 10.1103/PhysRevLett.128.231802. URL: https://link.aps.org/doi/ 10.1103/PhysRevLett.128.231802.

- [21] Boris Korzh et al. "Demonstration of sub-3 ps temporal resolution with a superconducting nanowire single-photon detector". en. In: *Nat. Photonics* 14.4 (Apr. 2020), pp. 250–255.
- [22] V B Verma et al. "Single-photon detection in the mid-infrared up to 10 m wavelength using tungsten silicide superconducting nanowire detectors". en. In: *APL Photonics* 6.5 (2021), p. 056101.
- [23] Marco Colangelo et al. "Large-area superconducting nanowire single-photon detectors for operation at wavelengths up to 7.4 m". en. In: *Nano Lett.* 22.14 (July 2022), pp. 5667–5673.
- [24] Gregor G Taylor et al. "Low-noise single-photon counting superconducting nanowire detectors at infrared wavelengths up to 29 µm". en. In: Optica 10.12 (Dec. 2023), p. 1672.
- [25] Jascha A Lau et al. "Superconducting single-photon detectors in the mid-infrared for physical chemistry and spectroscopy". en. In: *Chem. Soc. Rev.* 52.3 (Feb. 2023), pp. 921–941.
- [26] Sahil R Patel et al. "Improvements of readout signal integrity in mid-infrared superconducting nanowire single-photon detectors". en. In: *Appl. Phys. Lett.* 124.16 (Apr. 2024).
- [27] Fumihiro China et al. "Highly efficient NbTiN nanostrip single-photon detectors using dielectric multilayer cavities for a 2-μm wavelength band". en. In: *Opt. Express* 31.12 (June 2023), pp. 20471–20479.
- [28] Jin Chang et al. "Efficient mid-infrared single-photon detection using superconducting NbTiN nanowires with high time resolution in a Gifford-McMahon cryocooler". en. In: *Photonics Res.* 10.4 (Apr. 2022), p. 1063.
- [29] Hui Zhou et al. "Superconducting nanowire single photon detector with efficiency over 60% for 2-m-wavelength". In: *IEEE Photonics J.* 11.6 (Dec. 2019), pp. 1–7.
- [30] Michelle Brann, Varun Verma, and Solomon Woods. "Calibration system for mid-infrared superconducting nanowire single photon detectors". In: *Infrared Sensors, Devices, and Appli*cations XIII. Ed. by Ashok K Sood, Priyalal Wijewarnasuriya, and Arvind I D'Souza. SPIE, Oct. 2023.
- [31] L Maingault et al. "Spectral dependency of superconducting single photon detectors". en. In: J. Appl. Phys. 107.11 (June 2010), p. 116103.
- [32] D Henrich et al. "Broadening of hot-spot response spectrum of superconducting NbN nanowire single-photon detector with reduced nitrogen content". In: *Journal of Applied Physics* 112 (July 2012), p. 074511.
- [33] Hiroyuki Shibata et al. "Ultimate low system dark-count rate for superconducting nanowire single-photon detector". en. In: *Opt. Lett.* 40.14 (July 2015), pp. 3428–3431.
- [34] Hiroyuki Shibata et al. "SNSPD with ultimate low system dark count rate using various cold filters". In: *IEEE Trans. Appl. Supercond.* 27.4 (June 2017), pp. 1–4.
- [35] Yujun Zhong et al. "Review of mid-infrared plasmonic materials". In: *J. Nanophotonics* (Feb. 2015).
- [36] Huakang Yu et al. "Plasmon-enhanced light–matter interactions and applications". en. In: *Npj Comput. Mater.* 5.1 (Apr. 2019).
- [37] Anatoly V Zayats, Igor I Smolyaninov, and Alexei A Maradudin. "Nano-optics of surface plasmon polaritons". en. In: *Phys. Rep.* 408.3-4 (Mar. 2005), pp. 131–314.
- [38] Lei Feng et al. "Photonic metamaterial absorbers: Morphology engineering and interdisciplinary applications". en. In: Adv. Mater. 32.27 (July 2020), e1903787.
- [39] Philipp Karl et al. "Niobium nitride plasmonic perfect absorbers for tunable infrared superconducting nanowire photodetection". en. In: *Opt. Express* 29.11 (May 2021), pp. 17087–17096.
- [40] Jihua Zou et al. "Broadband mid-infrared perfect absorber using fractal Gosper curve". In: J. Phys. D Appl. Phys. 53.10 (Mar. 2020), p. 105106.
- [41] Aleksandar D. Rakić et al. "Optical properties of metallic films for vertical-cavity optoelectronic devices". In: *Appl. Opt.* 37.22 (Aug. 1998), pp. 5271-5283. DOI: 10.1364/AO.37.005271. URL: https://opg.optica.org/ao/abstract.cfm?URI=ao-37-22-5271.

- [42] L Gao, F Lemarchand, and M Lequime. "Refractive index determination of SiO₂ layer in the UV/Vis/NIR range: spectrophotometric reverse engineering on single and bi-layer designs". en. In: J. Eur. Opt. Soc. Rapid Publ. 8.13010 (2013), p. 13010.
- [43] A I Golovashkin et al. "OPTICAL PROPERTIES OF NIOBIUM." In: Zh. Eksp. Teor. Fiz., 56: 51-64(Jan. 1969). (Dec. 1968). URL: https://www.osti.gov/biblio/4811756.
- [44] J McVay, A Hoorfar, and N Engheta. "Thin absorbers using space-filling-curve high-impedance surfaces". In: 2005 IEEE Antennas and Propagation Society International Symposium. IEEE, 2005.
- [45] Yun Meng et al. "Fractal superconducting nanowires detect infrared single photons with 84% system detection efficiency, 1.02 polarization sensitivity, and 20.8 ps timing resolution". en. In: ACS Photonics 9.5 (May 2022), pp. 1547–1553.
- [46] Ilya A Stepanov et al. "Sputtered NbN films for ultrahigh performance superconducting nanowire single-photon detectors". en. In: *APL Mater.* 12.2 (Feb. 2024).
- [47] Andrew E. Dane. "Reactive DC magnetron sputtering of ultrathin superconducting niobium nitride films". In: 2015. URL: https://api.semanticscholar.org/CorpusID:109377179.
- [48] Yachin Ivry et al. "Universal scaling of the critical temperature for thin films near the superconducting-to-insulating transition". In: *PHYSICAL REVIEW B 90, 214515 (2014)* (Dec. 2014).
- [49] Nicola Pinto et al. "Dimensional crossover and incipient quantum size effects in superconducting niobium nanofilms". en. In: Sci. Rep. 8.1 (Mar. 2018), p. 4710.